

KiDS-1000: Detection of deviations from a purely cold dark-matter power spectrum with tomographic weak gravitational lensing

Patrick Simon^{1*}, Lucas Porth¹, Pierre Burger^{2,3,1}, and Konrad Kuijken⁴

¹Argelander-Institut für Astronomie, Universität Bonn, Auf dem Hügel 71, 53121 Bonn, Germany

²Waterloo Centre for Astrophysics, University of Waterloo, Waterloo, ON N2L 3G1, Canada

³Department of Physics and Astronomy, University of Waterloo, Waterloo, ON N2L 3G1, Canada

⁴Leiden Observatory, Leiden University, Einsteinweg 55, 2333 CC Leiden, The Netherlands

Received February 10, 2025

ABSTRACT

Model uncertainties in the nonlinear structure growth limit current probes of cosmological parameters. To shed more light on the physics of nonlinear scales, we reconstruct the finely binned three-dimensional power-spectrum from lensing data of the Kilo-Degree Survey (KiDS), relying solely on the background cosmology, source redshift distributions, and the intrinsic alignment (IA) amplitude of sources (and their uncertainties). The adopted Tikhonov regularisation stabilises the deprojection, enabling a Bayesian reconstruction in separate z -bins. Following a detailed description of the algorithm and performance tests with mock data, we present our results for the power spectrum as relative deviations from a Λ CDM reference spectrum that includes only structure growth by cold dark matter. Averaged over the full range $z \lesssim 1$, a *Planck*-consistent reference then requires a significant suppression on nonlinear scales, $k = 0.05\text{--}10 h \text{Mpc}^{-1}$, of up to 20%–30% to match KiDS-1000 (68% credible interval, CI, throughout). Conversely, a reference with a lower $S_8 \approx 0.73$ avoids suppression and matches the KiDS-1000 spectrum within a 20% tolerance. When resolved into three z -bins, however, and regardless of the reference, we detect structure growth only between $z \approx 0.4\text{--}0.13$, but not between $z \approx 0.7\text{--}0.4$. This could indicate spurious systematic errors in KiDS-1000, inaccuracies in the intrinsic alignment (IA) model, or potentially a non-standard cosmological model with delayed structure growth. In the near future, analysing data from stage-IV surveys with our algorithm promises a substantially more precise reconstruction of the power spectrum.

Key words. gravitational lensing: weak – large-scale structure of the Universe – cosmology: observations

1. Introduction

In contrast to the continuous background expansion of the Universe, the structure growth in the matter density field is less certain, with theoretical uncertainties varying by 10% or more in the nonlinear regime through their dependence on baryon-galaxy feedback, possible deviations from a purely cold, stable, and interaction-free dark-matter, or, perhaps, modifications in the standard model of gravity (e.g., Laguë et al. 2024; Bucko et al. 2024; Mauland et al. 2024; Ferreira et al. 2024; Salcido et al. 2023; Schneider et al. 2022; Harnois-Déraps et al. 2015; Smith & Markovic 2011; Jing et al. 2006, and references therein). Currently the theory uncertainties are limiting studies of cosmological parameters because they often rely on measures of the cosmic structure, such as the matter power spectrum, $P_\delta(k, z)$, at different redshift, $z =: 1/a - 1$, and spatial (comoving) wave number, k (e.g., Pranjali et al. 2024; García-García et al. 2024; Secco et al. 2022; Li et al. 2023; Asgari et al. 2021; Heymans et al. 2013). To shed more light on the physics imprinted on nonlinear scales, direct measurements of a model-free $P_\delta(k, z)$ with a minimum of assumptions promise to be a valuable model test. That this is already feasible for $z \lesssim 1$ and $10^{-2} \lesssim k/(h \text{Mpc}^{-1}) \lesssim 10$ with stage-III galaxy surveys when exploiting the weak gravitational lensing effect, such as with KiDS-1000 (Kuijken et al. 2019, 2015), is shown in this work. This foreshadows exciting applications to future lensing data, such as those by *Euclid* (Euclid Collaboration: Mellier et al. 2024), the *Vera C. Rubin* Ob-

servatory Legacy Survey of Space and Time (The LSST Dark Energy Science Collaboration et al. 2018), or the *Nancy Grace Roman* Space Telescope (Spergel et al. 2015).

The coherent distortion of distant galaxy images, just sources hereafter, by the weak shearing of light bundles passing through intervening foreground structure probes the matter power spectrum (e.g., for a review: Kilbinger 2015, Schneider 2006, Bartelmann & Schneider 2001). More specifically, and putting negligible higher-order corrections aside (Hilbert et al. 2009), the second-order correlations, $\xi_\pm(\theta)$, at lag θ in the cosmic shear field are simply a linear projection of $P_\delta(k, z)$ throughout the look-back light cone up to the distance of the sources (Preston et al. 2024; Mezzetti et al. 2012; Simon 2012; Bacon et al. 2005; Pen et al. 2003; Tegmark & Zaldarriaga 2002; Seljak 1998). Therefore, by using $\xi_\pm^{(ij)}(\theta)$ between tomographic bins, i and j , for different characteristic distances of sources, the correlation data can be deprojected to recover, within limitations, the original $P_\delta(k, z)$. More conveniently, as in Simon (2012, S12), we focus on a transfer function, $f_\delta(k, z) = P_\delta(k, z)/P_\delta^{\text{fid}}(k, z)$, with respect to a reference model, $P_\delta^{\text{fid}}(k, z)$, to highlight deviations from the presumed reference inside an average z -bin. For this reference, we choose a purely cold dark-matter (CDM) model to probe for deviations, $f_\delta(k, z) \neq 1$, that may hint at missing physics in a basic, well-understood dark-matter scenario or at unidentified systematic errors in the data. But, at the end of the day, the kind of reference is a deliberate choice.

Required for the deprojection, on the other hand, is the knowledge of the projection (lensing) kernel and the inclusion

* e-mail: psimon@astro.uni-bonn.de

of the intrinsic alignment (IA) of sources in the correlation function, an essential part of modern cosmic-shear analyses (Hirata & Seljak 2004; Crittenden et al. 2001; Croft & Metzler 2000). The lensing kernel is fully described by the radial distribution of sources inside the tomographic bins, the average matter density in today’s Universe, Ω_m , relative to the critical density, $\rho_{\text{crit}} = 3H_0^2(8\pi G_N)^{-1}$, and the expansion rate $E(a) := H_0^{-1}\dot{a}/a$, where $H_0 = 100 h \text{ km s}^{-1} \text{ Mpc}^{-1}$ is the Hubble constant and G_N Newton’s gravitational constant. The kernel parameters Ω_m and $E(a)$ are confined to percentage precision by cosmological experiments already ($E^2(a) \approx \Omega_m[a^{-3} - 1] + 1$ for a flat universe), especially owing to CMB experiments (Planck Collaboration et al. 2020; Hinshaw et al. 2013) but also by combining probes from the closer Universe (e.g., Heymans et al. 2021; Abbott et al. 2018). Nevertheless, in the refinement of the method in S12 for KiDS-1000, we marginalise here over the small background cosmology uncertainties, as well as over those in the source distributions (Hildebrandt et al. 2021). Another refinement is the required inclusion of the IA, and its uncertainty, in the deprojection procedure by the widely employed nonlinear alignment (NLA) model (Joachimi et al. 2011; Bridle & King 2007), informed by IA constraints in KiDS-1000 (Asgari et al. 2021).

Despite the simplicity of the well-defined projection, the noise level in $\xi_{\pm}^{(ij)}(\theta)$ makes the recovery of the matter power spectrum still challenging because the deprojection has to undo a convolution in radial and transverse direction, producing strongly correlated, oscillating noise in an unstable reconstruction. This complication could be mitigated by data volumes substantially larger than KiDS-1000, beating down oscillating noise, or by additional assumptions on the redshift dependence or shape of the power spectrum in fitting an analytical model with few parameters to the data (Ye et al. 2024; Truttero et al. 2024; Broxterman & Kuijken 2024; Preston et al. 2024, 2023; Pen et al. 2003; Seljak 1998). Avoiding analytical models, we instead propose to constrain $f_{\delta}(k, z)$ averages in different k - and z -bins, as in S12 but additionally filtered by a classic Tikhonov regularisation, as, for instance, applied in the mathematically related problem of deconvolving noisy images (e.g., Murata & Takeuchi 2022). In contrast to S12, the Tikhonov regularisation, installed on our Bayesian statistical model as prior, penalises strongly oscillating power spectra for noisy data, giving an advantage to solutions of $f_{\delta}(k, z)$ that, on the one hand, are smoother in k -direction but, on the other hand, use no prior information on their z -dependence. We show with verification data that this regularisation indeed stabilises the reconstruction and extracts from KiDS-1000 data useful constraints on the transfer function $f_{\delta}(k, z)$, either averaged over the full redshift range or averaged within three separate redshift bins to broadly probe a redshift evolution. Furthermore, for an efficient sampling of the posterior constraints of the matter power spectrum, we describe and test a Monte-Carlo Markov Chain (MCMC) code tailored to deal with the numerous 60 (or more) degrees-of-freedom of the binned, band power $P_{\delta}(k, z)$; its practical details are given in Appendix A.

The outline of the paper is as follows. Section 2 reviews our weak lensing formalism and shows that the projection of $P_{\delta}(k, z)$ into $\xi_{\pm}^{(ij)}(\theta)$, both binned, can be reduced to one projection matrix, to be reused as long as the same lensing kernel and IA parameters, including source redshift distributions, are employed. Section 3 defines the statistical model for our Bayesian analysis, including a prior for the Tikhonov regularisation. We summarise the KiDS-1000 data for our cosmic shear analysis in Sect. 4 and report our results in Sect. 5. Section 5 also reports, as verification of our reconstruction method, results of a mock analysis based

on KiDS-1000-like data produced by ray-tracing N -body data. Another verification test, this time based on the data vector of an analytical model subject to random noise, is presented in Appendix A. We discuss our results and conclusions on the reconstructed matter power spectrum in Sect. 6. Notably, our figures use comoving wave numbers, k , for spatial scales of the matter power spectrum, stressed by the ‘c’ in the unit $[k] = h \text{ cMpc}^{-1}$.

2. Weak lensing formalism

This work is an application of the well-established theory of cosmic shear. For a review and its mathematical foundation, we refer to Kilbinger (2015) or Schneider (2006), and only briefly summarise our formalism here.

2.1. Cosmic shear

Weak gravitational lensing by fluctuations in the large-scale structure of the foreground matter density, $\delta_m = \rho_m/\bar{\rho}_m - 1$, distorts images of background galaxies. Their average shear distortion in direction θ of the sky shall be expressed by the complex $\gamma(\theta) = \gamma_1(\theta) + i\gamma_2(\theta)$ for an ensemble of galaxies with probability distribution function (PDF) $p_{\chi}(\chi)$ in comoving distance, χ . To lowest order, and sufficiently accurate in practical applications, the Fourier transform $\tilde{\gamma}(\ell)$ is related to the linear projection of fluctuations along θ ,

$$\kappa(\theta) = \frac{3H_0^2 \Omega_m}{2c^2} \int_0^{\chi_h} \frac{d\chi}{a(\chi)} \overline{W}(\chi) f_k(\chi) \delta_m[f_k(\chi)\theta, \chi], \quad (1)$$

through the convolution ($\ell \neq 0$)

$$\tilde{\gamma}(\ell) = \int_{\mathbb{R}^2} d^2\theta \gamma(\theta) \exp(-i\theta \cdot \ell) = \frac{(\ell_1 + i\ell_2)^2}{\ell^2} \tilde{\kappa}(\ell), \quad (2)$$

where c is the vacuum speed of light. In the above equations, $\tilde{\kappa}(\ell)$ is the Fourier transform of the convergence $\kappa(\theta)$, the scalar $f_k(\chi)$ is the (comoving) angular diameter distance for the curvature scalar K , the vector $f_k(\chi)\theta$ denotes a separation in a tangential plane on the sky at distance χ , the term $1 + z = a^{-1}(\chi)$ is our relation between redshift, z , and scale factor, $a(\chi)$, at the look back time of χ , and

$$\overline{W}(\chi) := \int_{\chi}^{\chi_h} d\chi' p_{\chi}(\chi') \frac{f_k(\chi' - \chi)}{f_k(\chi')} \quad (3)$$

is the lensing efficiency, cut off at the size of the observable Universe, χ_h . As approximation, we assume a flat sky with Cartesian coordinates for θ but expect negligible inaccuracies for angular separations below several degrees.

Practical estimators of $\gamma(\theta)$ in the direction θ of a galaxy image use a convenient definition of galaxy ellipticity, ϵ , that is calibrated to be an unbiased estimator, $\langle \epsilon \rangle = \gamma$, for a selected source population (e.g., Giblin et al. 2021).

2.2. Second-order statistics

Our analysis exploits the coherent shear distortion of galaxy images over the sky to infer the three-dimensional power spectrum, $P_{\delta}(k, z)$, of matter density fluctuations inside the light cone,

$$\langle \tilde{\delta}_m(\mathbf{k}, z) \tilde{\delta}_m^*(\mathbf{k}', z) \rangle =: (2\pi)^3 \delta_D(\mathbf{k} - \mathbf{k}') P_{\delta}(k, z), \quad (4)$$

for a range of wave numbers and redshifts. The $\delta_D(\mathbf{x})$ denotes the Dirac delta function, and $\tilde{\delta}_m(\mathbf{k}, z)$ is the Fourier coefficient of a

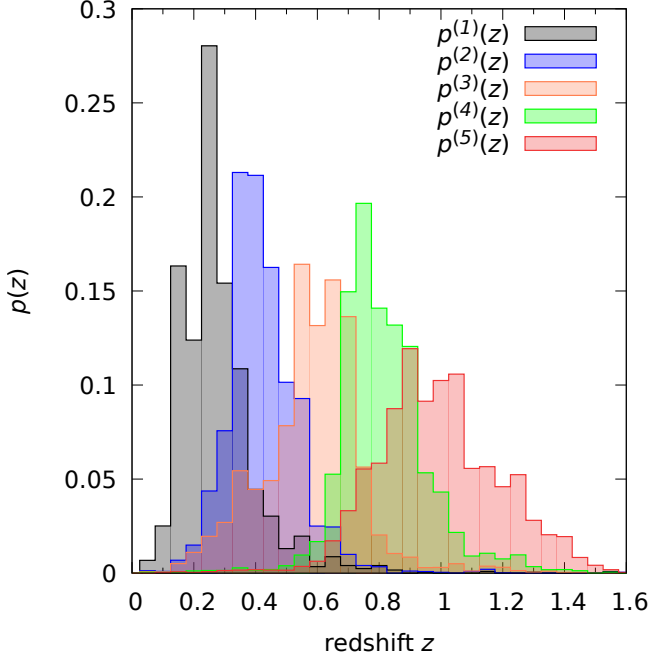


Fig. 1. Probability density distribution functions, $p_z^{(i)}(z)$, of KiDS-1000 source galaxies within the five tomographic redshift bins (from $i = 1$ to $i = 5$): (0.1, 0.3], (0.3, 0.5], (0.5, 0.7], (0.7, 0.9], and (0.9, 1.2]. These estimates are taken from Hildebrandt et al. (2021).

fluctuation mode at redshift z inside the light cone. To obtain the power spectrum from $\gamma(\theta)$, we estimate the two-point correlation function of cosmic shear,

$$\xi_{\pm}(\theta) := \langle \gamma_t(\theta_1) \gamma_t(\theta_2) \rangle \pm \langle \gamma_{\times}(\theta_1) \gamma_{\times}(\theta_2) \rangle \quad (5)$$

at lag $\theta = |\theta_2 - \theta_1|$ from an ensemble of sources. Here, γ_t and γ_{\times} denote the tangential and cross shear components relative to the orientation of $\theta_2 - \theta_1 =: \theta e^{i\phi}$ on the sky, defined by $\gamma_t + i\gamma_{\times} := -e^{-2i\phi}\gamma$. In addition, using the hybrid extended Limber approximation in Fourier space (Kilbinger et al. 2017; Kaiser 1992), the correlation function of cosmic shear is a linear projection of $P_{\delta}(k, z)$,

$$\xi_{\pm}(\theta) = \frac{9H_0^4 \Omega_m^2}{4c^4} \int_0^{\chi_h} \int_0^{\infty} \frac{d\chi d\ell \ell}{2\pi} \frac{\bar{W}^2(\chi)}{a^2(\chi)} J_{0,4}(\ell\theta) P_{\delta}\left(\frac{\ell + 1/2}{f_{\kappa}(\chi)}, \chi\right) \quad (6)$$

through the lensing kernel $K(\chi) \propto \Omega_m^2 \bar{W}^2(\chi) a^{-2}(\chi)$ – the minimal ingredient that has to be known to invert the projection. The expressions $J_n(x)$ denote n^{th} -order Bessel functions of the first kind, of which $J_0(x)$ has to be applied for ξ_+ and $J_4(x)$ for ξ_- .

2.3. Tomographic lensing and intrinsic alignment of sources

Owing to the information loss in the projection Eq. (6) for a single sample of sources, a power spectrum averaged over the entire light cone could be obtained at best, as in Pen et al. (2003) or Schneider et al. (2002). More advanced is splitting the source samples by redshift in a tomographic analysis for a better statistical precision, reflected by improved cosmology constraints in tomographic analyses, or to achieve a (limited) redshift resolution

for the recovered $P_{\delta}(k, z)$. Therefore, we split our source sample into five redshift bins, using non-overlapping ranges of photometric redshifts, namely the z_B -intervals (0.1, 0.3], (0.3, 0.5], (0.5, 0.7], (0.7, 0.9], and (0.9, 1.2], as done already in Hildebrandt et al. (2021). Figure 1 plots estimates of the resulting distributions $p_z^{(i)}(z)$ for each bin i . The tomographic analysis then correlates the shear signal between bins i and j , denoted by the superscript “ (ij) ” in $\xi_{\pm}^{(ij)}(\theta)$. Compared to Eq. (6), this increases the data vector size by a factor of $5(5 + 1)/2 = 15$ but also adds information on the $P_{\delta}(k, z)$ evolution because the shear tomography probes the same foreground with sources at different z .

This tomographic analysis requires special attention towards additional contributions to the shear signal from the intrinsic alignment (IA) of sources (e.g., Lamman et al. 2024). In the ideal absence of IA, the orientations of intrinsic source ellipticities are statistically independent among each other and to the cosmic shear signal. So-called ‘II’ contributions, however, originate from correlated orientations of physically close galaxies. In addition, galaxy shapes are aligned to the surrounding matter density, giving rise to a ‘GI’ signal (Hirata & Seljak 2004). While II contributions could in principle be reduced by correlating only bin combinations with little radial overlap, and the GI signal could be suppressed by a nulling technique (Joachimi & Schneider 2008), we follow the common approach of modelling the II and GI signal in $\xi_{\pm}^{(ij)}(\theta)$ to avoid information loss,

$$\xi_{\pm}^{(ij)}(\theta) = {}^0\xi_{\pm}^{(ij)}(\theta) + {}^{\text{II}}\xi_{\pm}^{(ij)}(\theta) + {}^{\text{GI}}\xi_{\pm}^{(ij)}(\theta). \quad (7)$$

In this equation,

$${}^0\xi_{\pm}^{(ij)}(\theta) := \frac{9H_0^4 \Omega_m^2}{4c^4} \times \int_0^{\chi_h} \int_0^{\infty} \frac{d\chi d\ell \ell}{2\pi} \frac{\bar{W}^{(i)}(\chi) \bar{W}^{(j)}(\chi)}{a^2(\chi)} J_{0,4}(\ell\theta) P_{\delta}\left(\frac{\ell + 1/2}{f_{\kappa}(\chi)}, \chi\right) \quad (8)$$

is the ideal shear signal without IA. Covering both auto- ($i = j$) and cross-correlations ($i \neq j$) of source samples, this expression is more general than Eq. (6). Herein, the lensing efficiency with superscript, $\bar{W}^{(i)}(\chi)$, refers to Eq. (3) but for the PDF $p_{\chi}^{(i)}(\chi)$ of the i th bin. Notably, the $p_{\chi}^{(i)}(\chi)$ are related to the $p_z^{(i)}(z)$ in Fig. 1 by $p_{\chi}^{(i)}(\chi) = p_z^{(i)}[z(\chi)] |dz/d\chi|$ for $dz/d\chi = H_0 c^{-1} E[(1+z)^{-1}]$.

For the II and GI terms, we employ the NLA model by Joachimi et al. (2011), derived from the linear alignment model by Bridle & King (2007) but replacing the linear matter power-spectrum by the nonlinear one. Clearly just tweaking the original linear IA model, the NLA is nevertheless sufficiently accurate to model contemporary lensing data (Harnois-Déraps et al. 2022), predicting

$${}^{\text{II}}\xi_{\pm}^{(ij)}(\theta) := \int_0^{\chi_h} \int_0^{\infty} \frac{d\chi d\ell \ell}{2\pi} F^2(\chi) \times \frac{p_{\chi}^{(i)}(\chi) p_{\chi}^{(j)}(\chi)}{f_{\kappa}^2(\chi)} J_{0,4}(\ell\theta) P_{\delta}\left(\frac{\ell + 1/2}{f_{\kappa}(\chi)}, \chi\right) \quad (9)$$

for II correlations and for the GI term

$${}^{\text{GI}}\xi_{\pm}^{(ij)}(\theta) := \frac{3H_0^2 \Omega_m}{2c^2} \int_0^{\chi_h} \int_0^{\infty} \frac{d\chi d\ell \ell}{2\pi} F(\chi) \times \frac{\bar{W}^{(i)}(\chi) p_{\chi}^{(j)}(\chi) + \bar{W}^{(j)}(\chi) p_{\chi}^{(i)}(\chi)}{a(\chi) f_{\kappa}(\chi)} J_{0,4}(\ell\theta) P_{\delta}\left(\frac{\ell + 1/2}{f_{\kappa}(\chi)}, \chi\right). \quad (10)$$

The amplitude of the IA signal scales in this model with

$$F(\chi) = -A_{\text{IA}} C_1 \rho_{\text{crit}} \frac{\Omega_m}{D_+(\chi)} \approx -2.4 \times 10^{-2} \left(\frac{A_{\text{IA}}}{3.0}\right) \left(\frac{\Omega_m}{0.3}\right) \left(\frac{D_+(\chi)}{0.5}\right)^{-1} \quad (11)$$

and depends on distance χ (or redshift) only through the linear growth factor, $D_+(\chi)$ (by definition $D_+ \equiv 1$ at $\chi = 0$). For our main result, we neglect further dependencies on redshift or the evolution of the average galaxy luminosity with redshift, similar to Asgari et al. (2021) who find in their cosmological analysis of KiDS-1000 little evidence for a more complex $F(\chi)$.

With respect to future applications, the work by Fortuna et al. (2021), and, more recently, by Preston et al. (2024) observe that the NLA model, even if overly simplistic, could be accurate enough to model IA in stage-IV survey data if a redshift dependence of the NLA parameters is accounted for. We briefly return to this topic in our discussion on conceivable systematic uncertainties in our analysis in Sect. 6.

2.4. Projection kernels of the matter power spectrum

The shear correlation function with IA terms, Eq. (7), is still linear in the matter power spectrum, hence a deprojection of $\xi_{\pm}^{(ij)}(\theta)$ into $P_{\delta}(k, z)$ is, as in S12, principally possible through linear minimum-variance estimators that depend only on the background fiducial cosmology, source distributions, and IA parameters. On the practical side, however, the deprojection is hampered by broad, partly similar lensing kernels, the relatively low signal-to-noise ratio, and a confined θ -range, rendering the estimators ill-conditioned (or singular). They are also biased when ignoring the θ -confinement which amounts to setting $\xi_{\pm}^{(ij)}(\theta) \equiv 0$ outside the θ range (Section 7 in Schneider et al. 2002). Similar to S12, we address these practicalities by boundary conditions $P_{\delta}(k, z) \geq 0$ through priors in the framework of a Bayesian analysis, at most a couple of redshift bins for $P_{\delta}(k, z)$, and by varying $P_{\delta}(k, z)$ within a confined region in (k, z) -space only, assuming a reference power, $P_{\delta}^{\text{fid}}(k, z)$, otherwise. Additionally, it is sensible to constrain the relative deviations $f_{\delta}(k, z) := P_{\delta}(k, z)/P_{\delta}^{\text{fid}}(k, z)$ instead of $P_{\delta}(k, z)$ directly: Most of the evolution is probably already accounted for in $P_{\delta}^{\text{fid}}(k, z)$, and a slowly changing $f_{\delta}(k, z)$ within a broad z -bin is a reasonable quantity to be averaged. We describe the implementation details below.

In our setup, the $f_{\delta}(k, z)$ shall be constant within cells of a regular mesh of $(N_k + 1) \times (N_z + 1)$ mesh points (k_m, χ_n) , where $k_m < k_{m+1}$, $z_n < z_{n+1}$, and $\chi_n := \chi(z_n)$; the intervals $[z_1, z_{N_z+1})$ and $[k_1, k_{N_k+1})$ define the z - and k -ranges where the power spectrum may differ from $P_{\delta}^{\text{fid}}(k, z)$, here for $k/(h \text{ Mpc}^{-1}) \in [10^{-2}, 20)$ and $z \in [0, 2)$. The matter power spectrum for Eq. (7) thus equals

$$P_{\delta}(k, \chi) = P_{\delta}^{\text{fid}}(k, \chi) \left(1 + \sum_{n,m=1}^{N_z, N_k} H_{mn}(k, \chi) [f_{\delta, mn} - 1] \right), \quad (12)$$

where

$$H_{mn}(k, \chi) := \begin{cases} 1 & , \text{ if } k \in [k_m, k_{m+1}) \text{ and } \chi \in [\chi_n, \chi_{n+1}) \\ 0 & , \text{ otherwise} \end{cases} \quad (13)$$

is a two-dimensional top-hat function. The average of $f_{\delta}(k, z)$ within a cell (or band) is denoted by the coefficient $f_{\delta, mn}$. The mesh in k -direction is equi-spaced on a log-scale, $\Delta k = k N_k^{-1} \ln(k_{N_k+1}/k_1)$, while the z -direction uses for one variant

$z_n \in \{0, 0.3, 0.6, 2\}$, for $N_z = 3$, and $z_n \in \{0, 2\}$ in other variant with one wide bin, $N_z = 1$, when averaging $f_{\delta}(k, z)$ over the entire redshift range.

Using this $f_{\delta, mn}$ -representation of $P_{\delta}(k, z)$, Eq. (7) is now recast into

$$\xi_{\pm}^{(ij)}(\theta) = \sum_{n,m=1}^{N_z, N_k} X_{\pm}^{(ij)}(\theta; m, n) f_{\delta, mn} + \xi_{\pm, \text{fid}}^{(ij)}(\theta), \quad (14)$$

for the projection matrix

$$X_{\pm}^{(ij)}(\theta; m, n) := \frac{1}{2\pi \theta^2} \int_{\chi_n}^{\chi_{n+1}} d\chi \left({}^0\mathcal{K}_{\gamma\gamma}^{(ij)}(\chi) + {}^{\text{II}}\mathcal{K}_{\gamma\gamma}^{(ij)}(\chi) + {}^{\text{GI}}\mathcal{K}_{\gamma\gamma}^{(ij)}(\chi) \right) \times \int_{k_m f_k(\chi)\theta}^{k_{m+1} f_k(\chi)\theta} ds s J_{0,4}(s) P_{\delta}^{\text{fid}}(k[s, \chi, \theta], \chi), \quad (15)$$

the integral kernels

$${}^0\mathcal{K}_{\gamma\gamma}^{(ij)}(\chi) := \frac{9H_0^4 \Omega_m^2}{4c^4} \frac{\overline{W}^{(i)}(\chi) \overline{W}^{(j)}(\chi)}{a^2(\chi)}; \quad (16)$$

$${}^{\text{II}}\mathcal{K}_{\gamma\gamma}^{(ij)}(\chi) := F^2(\chi) \frac{p_{\chi}^{(i)}(\chi) p_{\chi}^{(j)}(\chi)}{f_k^2(\chi)}; \quad (17)$$

$${}^{\text{GI}}\mathcal{K}_{\gamma\gamma}^{(ij)}(\chi) := \frac{3H_0^2 \Omega_m}{2c^2} F(\chi) \times \frac{\overline{W}^{(i)}(\chi) p_{\chi}^{(j)}(\chi) + \overline{W}^{(j)}(\chi) p_{\chi}^{(i)}(\chi)}{a(\chi) f_k(\chi)}, \quad (18)$$

and a constant offset

$$\xi_{\pm, \text{fid}}^{(ij)}(\theta) := \frac{1}{2\pi \theta^2} \int_0^{\chi_h} d\chi \left({}^0\mathcal{K}_{\gamma\gamma}^{(ij)}(\chi) + {}^{\text{II}}\mathcal{K}_{\gamma\gamma}^{(ij)}(\chi) + {}^{\text{GI}}\mathcal{K}_{\gamma\gamma}^{(ij)}(\chi) \right) \times \int_0^{\infty} ds s J_{0,4}(s) P_{\delta}^{\text{fid}}(k[s, \chi, \theta], \chi) \quad (19)$$

from (k, z) regions that are unaffected by the choice of $f_{\delta, mn}$. The offset employs the definition

$$P_{\delta}^{\text{fid}}(k, \chi) := \begin{cases} P_{\delta}^{\text{fid}}(k, \chi) & , \text{ if } \sum_{m,n=1}^{N_z, N_k} H_{mn}(k, \chi) = 0 \\ 0 & , \text{ otherwise} \end{cases}, \quad (20)$$

and the foregoing equations abbreviate $k[s, \chi, \theta] := \frac{s+\theta/2}{f_k(\chi)\theta}$.

Our code computes the projection matrix $X_{\pm}^{(ij)}(\theta; m, n)$ once for a series of θ -bins, enabling a quick prediction of $\xi_{\pm}^{(ij)}(\theta)$ when Monte-Carlo sampling the posterior PDF of $f_{\delta, mn}$. An efficient way to numerically calculate $X_{\pm}^{(ij)}(\theta; m, n)$ and $\xi_{\pm, \text{fid}}^{(ij)}(\theta)$ is given in Appendix A of S12, albeit with the little modification $(2f_k[\chi])^{-1}$ in what is now $\bar{k}_j := (2f_k[\chi])^{-1} + (\hat{k}_j + \hat{k}_{j+1})/2$ due to the extended hybrid Limber approximation adopted here. As further practical footnote on code implementation, we perform the above integrals with integration variable a instead of χ , as well as $p_z(z)$ instead of $p_{\chi}(\chi)$, for which the following transformations are notable, given a general function $g(\chi)$ and $H(a) =: H_0 E(a)$,

$$\int_{\chi_1}^{\chi_2} d\chi g(\chi) = \frac{c}{H_0} \int_{a_2}^{a_1} \frac{da}{a^2 E(a)} g[\chi(a)] \quad (21)$$

Table 1. Parameters of the reference power spectrum, $P_\delta^{\text{fid}}(k, z)$, and the projection parameters (lensing kernel, IA) used to infer $f_\delta(k, z) = P_\delta(k, z)/P_\delta^{\text{fid}}(k, z)$. For $P_\delta^{\text{fid}}(k, z)$ in this Λ CDM setting, we employ an updated version of `halofit` (Smith et al. 2003; Takahashi et al. 2012). The reference assumes a flat cosmology, this means $\Omega_\Lambda = 1 - \Omega_m$.

A_{IA}	Ω_m	Ω_b	n_s
+1.070	0.305	0.047	0.901
h	σ_8	Γ	w_0
0.695	0.720 [†]	0.167	-1.000

Notes. A_{IA} : IA amplitude of the NLA model; Ω_m : (total) matter density parameter; Ω_b : baryon density parameter; n_s : shape parameter of the primordial power spectrum; h : Hubble constant in units of $100 \text{ km s}^{-1} \text{ Mpc}^{-1}$; σ_8 : normalisation of the linear power spectrum at $z = 0$; Γ : shape parameter according to Sugiyama (1995); w_0 : equation-of-state parameter for dark energy; [†] this value has been lowered from the 0.76 in Heymans et al. (2021), Table C.1, to obtain an average of $f_\delta \approx 1$ over all k and z (Sect. 5.1)

since $|d\chi/da| = c/(a^2 H[a])$,

$$\int_{\chi_1}^{\chi_2} d\chi p_\chi^{(i)}(\chi) g(\chi) = \int_{a_2}^{a_1} \frac{da}{a^2} p_z^{(i)}[z(a)] g[\chi(a)] \quad (22)$$

since $|dz/d\chi| = H(z)/c$, and hence

$$\begin{aligned} \int_{\chi_1}^{\chi_2} d\chi p_\chi^{(i)}(\chi) p_\chi^{(j)}(\chi) g(\chi) \\ = \frac{H_0}{c} \int_{a_2}^{a_1} \frac{da}{a^2} E(a) p_z^{(i)}[z(a)] p_z^{(j)}[z(a)] g[\chi(a)]. \end{aligned} \quad (23)$$

When integrating over $p_z^{(i)}(z)$, we adopt histograms with top-hat functions, without interpolation, exactly as indicated in Fig. 1. The very first bin, left-aligned towards $z = 0$, has $p_z^{(i)}(z) = 0$. Probably obvious through these integrals and the pre-factors in Eqs. (8)–(10), the projections of $P_\delta(k, z)$ into $\xi^{(ij)}(\theta)$ are independent of H_0 as long as $[k] = h \text{ Mpc}^{-1}$ (comoving), whereas the $\xi_\pm^{(ij)}(\theta)$ scale with Ω_m^2 since $F(\chi) \propto \Omega_m$.

3. Bayesian inference of the three-dimensional matter power-spectrum

With the linear relation between the three-dimensional (3D) power spectrum and the two-point shear correlation functions described, we now outline the statistical model and the numerical sampler for the posterior probability density of $f_{\delta, mn}$ within a Bayesian framework (e.g., Gelman et al. 2003, for a review). In comparison to S12, our updated methodology introduces the Tikhonov regularisation as Bayesian prior, in effect inferring a k -smoothed power spectrum, and a Hamiltonian MCMC for improved computational speed for $N_z \times N_k \sim 60$ model variables.

3.1. Statistical model

The statistical model of $f_{\delta, mn}$ employs a compact notation for the tomographic data, model variables and parameters, all presented here. The vector of model variables $\boldsymbol{\pi} = (f_{\delta, mn} | 1 \leq n \leq N_z, 1 \leq m \leq N_k)$ compiles the bin-averaged $f_\delta(k, z)$ on a $(N_k + 1) \times (N_z + 1)$ mesh, and the data vector

\boldsymbol{d} contains the binned $\xi_\pm^{(ij)}(\theta_k)$ for a sequence of $N_\theta = 9$ angular separations, θ_k . Equation (14) predicts the components of \boldsymbol{d} for a given (flat) background cosmology, IA parameters, and source redshift distributions, altogether compressed into $\boldsymbol{q} = \{\Omega_m, A_{\text{IA}}, p_z^{(1)}(z), \dots, p_z^{(5)}(z)\}$ hereafter. The prediction is denoted by the model vector $\boldsymbol{m}(\boldsymbol{\pi}, \boldsymbol{q}) = \boldsymbol{X}_q \boldsymbol{\pi} + \boldsymbol{\xi}_q^{\text{fid}}$ with elements arranged in the same order as those in \boldsymbol{d} , using the projection matrix \boldsymbol{X}_q which contains the coefficients $X_\pm^{(ij)}(\theta; m, n)$ for fixed \boldsymbol{q} . The elements of $\boldsymbol{\xi}_q^{\text{fid}}$ are the offsets $\xi_{\pm, \text{fid}}^{(ij)}(\theta_k)$, also for fixed projection parameters \boldsymbol{q} . The statistical information on $\boldsymbol{\pi}$ is expressed by the Bayesian posterior PDF of $\boldsymbol{\pi}$ conditional on \boldsymbol{d} ,

$$P(\boldsymbol{\pi} | \boldsymbol{d}) = \mathcal{E}^{-1}(\boldsymbol{d}) \mathcal{L}_q(\boldsymbol{d} | \boldsymbol{\pi}) P_{\text{hat}}(\boldsymbol{\pi}) P_\tau(\boldsymbol{\pi}), \quad (24)$$

adopting a Gaussian likelihood

$$-2 \ln \mathcal{L}_q(\boldsymbol{d} | \boldsymbol{\pi}) = [\boldsymbol{d} - \boldsymbol{m}(\boldsymbol{\pi}, \boldsymbol{q})]^T \boldsymbol{C}^{-1} [\boldsymbol{d} - \boldsymbol{m}(\boldsymbol{\pi}, \boldsymbol{q})] \quad (25)$$

with error covariance \boldsymbol{C} of the measurement \boldsymbol{d} , and two prior probability densities, $P_{\text{hat}}(\boldsymbol{\pi})$ and $P_\tau(\boldsymbol{\pi})$, to regularise the sampling in f_δ -parameter space. The normalisation, $\mathcal{E}(\boldsymbol{d}) = \int d\boldsymbol{\pi} \mathcal{L}_q(\boldsymbol{d} | \boldsymbol{\pi}) P_{\text{hat}}(\boldsymbol{\pi}) P_\tau(\boldsymbol{\pi}) \neq 0$, is not of interest for the Monte-Carlo sampler, and hence we set $\mathcal{E}(\boldsymbol{d}) \equiv 1$ without impacting the results. We describe the two prior PDFs in the following.

3.2. Tikhonov regularisation prior

The Tikhonov regularisation prior, $P_\tau(\boldsymbol{\pi})$, greatly improves the constraints, pruning implausible solutions for $f_{\delta, mn}$. This is necessary because the combination of heavy smoothing and added noise in $\xi_\pm^{(ij)}(\theta)$ has the unpleasant side-effect of producing strong oscillations, correlated errors, in $f_\delta(k, z)$ when inverting the tomographic signal. Similar to 3D-lensing mass reconstructions (Hu & Keeton 2002), the oscillations are reduced by applying regularisation conditions. To this effect, the Tikhonov regularisation down-weights oscillating $f_\delta(k, z)$, preferring solutions of $f_{\delta, mn}$ smoothed in k -direction,

$$-\frac{1}{\tau} \ln P_\tau(\boldsymbol{\pi}) = \sum_{n=1}^{N_z} \sum_{m=1}^{N_k-1} (f_{\delta, mn} - f_{\delta, (m+1)n})^2. \quad (26)$$

At the same time, no prior constraints are imposed on the overall amplitude of $f_{\delta, mn}$ or the difference signal between z -bins because only signal differences from the same z -bin, n , appear inside the prior density. The weight of the prior relative to the data likelihood $\mathcal{L}_q(\boldsymbol{d} | \boldsymbol{\pi})$ is controlled by the Tikhonov parameter τ , demonstrated in Fig. 2 for a simulated analysis with three redshift bins, $N_z = 3$.

This intentionally extreme scenario in Fig. 2 highlights the impact of the regularisation with a truly z -evolving and scale-dependent $f_{\delta, mn}$ by choosing a constant reference $P_\delta^{\text{fid}}(k, z)$ for all z -bins: a theory power spectrum at $z = 1$. Unlike the actual KiDS analysis in Sect. 5, the $f_{\delta, mn}$ therefore now quantify the structure growth relative to $z = 1$. To assess the quality of the reconstruction and our ability to detect the z - and k -dependence of $f_{\delta, mn}$, we analyse a mock vector $\boldsymbol{d} = \boldsymbol{m}(\boldsymbol{\pi}, \boldsymbol{q})$ with parameters in Table 1 and KiDS-1000-like noise, \boldsymbol{C} , yielding posterior 68% credible regions with regularisation ($\tau = 5$, dark orange) and without ($\tau = 0$, light orange). The figure compares these credible regions to virtually noise-free data, unaffected by the Tikhonov regularisation, depicted as solid lines (“noise/100”). The solid lines are, to account for the z -weighting of $f_\delta(k, z)$ in a reconstruction, the posterior medians for a data vector with unrealistically high signal-to-noise ratio (S/N) of $\boldsymbol{C}' = 10^{-4} \times \boldsymbol{C}$

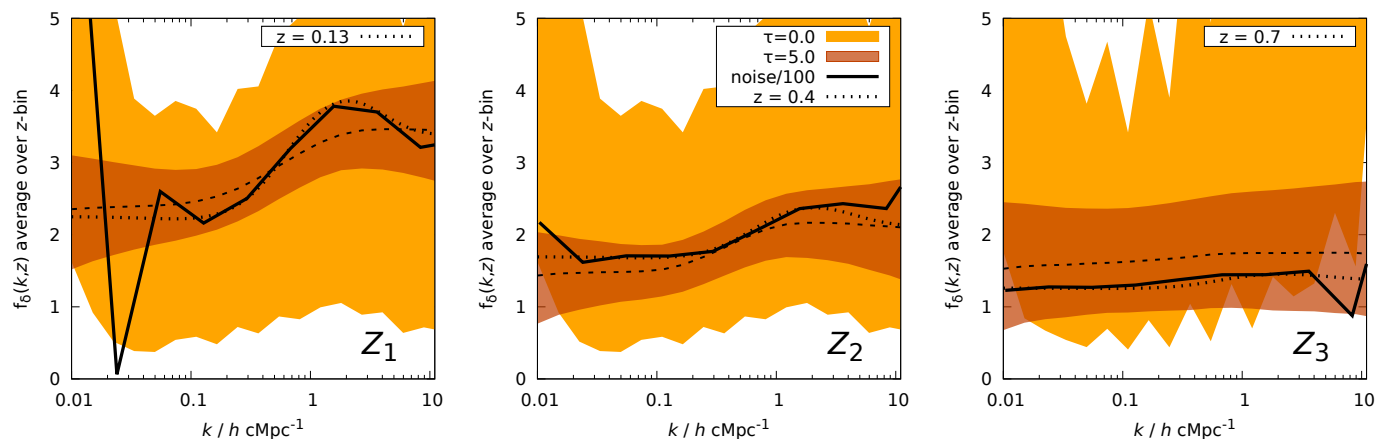


Fig. 2. Impact of the Tikhonov regularisation to suppress oscillating solutions $f_{\delta}(k, z)$. Shown are, for a noise-free mock data vector and the KiDS-1000 error covariance, the posterior constraints (68% credible regions) on f_{δ} averaged over the redshift bin $Z_1 = [0, 0.3]$ (left), $Z_2 = [0.3, 0.6]$ (middle), and $Z_3 = [0.6, 2]$ (right) with and without regularisation (dark orange $\tau = 5.0$ with median as dashed line, or light orange $\tau = 0$). To boost scale-dependence and evolution, $f_{\delta}(k, z)$ is here defined relative to the power spectrum at fixed redshift, probing the relative structure growth since $z = 1$. The solid line is the median posterior f_{δ} for 100 \times reduced measurement errors, providing a nearly noise-free reference (“noise/100”) that averages the growth over the redshift bin while still exhibiting artefacts near the edges. The dotted lines are the theoretical $P_{\delta}^{\text{fid}}(k, \bar{z})/P_{\delta}^{\text{fid}}(k, z = 1)$ for one specific \bar{z} chosen to match best the solid lines, indicating the redshift with highest weight in the average.

as error covariance and no Tikhonov regularisation. But even for such high-S/N data, artefacts appear towards large scales, close to $k \sim 0.02 h \text{Mpc}^{-1}$, and at the high- k end, near $k \sim 10 h \text{Mpc}^{-1}$, thus towards k where the tomographic data poorly constrain the power spectrum. To mitigate these artefacts, the additional dotted lines depict for each z -bin a theoretical $P_{\delta}^{\text{fid}}(k, \bar{z})/P_{\delta}^{\text{fid}}(k, z = 1)$ at one specific redshift, \bar{z} , that matches the solid lines best, and which shall be the ‘true’ average $f_{\delta, mn}$ for this experiment. Undoubtedly, a Tikhonov prior, $\tau = 5$, substantially reduces the statistical uncertainty in the reconstruction (sizes of credible regions for $\tau = 0$ versus $\tau = 5$). On the downside, however, the regularisation might be overly restrictive by straightening out oscillations actually present in the data, as already partly present for $\tau = 5$ (dotted lines versus dashed lines, the posterior median). By running more tests with different τ , not shown here, we consider $\tau = 5$ a good compromise that catches gradual trends with k while improving the precision in the reconstruction, as in the left panel. We reiterate that the degree of evolution and scale-dependence in this test, due to the static reference power spectrum, is extreme compared to what is expected in the KiDS-1000 analysis. If the reference is close to the true matter power at all z , $f_{\delta, mn}$ will be close to unity.

3.3. Positivity priors

Already applied for Fig. 2, we restrict valid solutions to positive $f_{\delta, mn}$ (since $P_{\delta}(k, z) \geq 0$), by using uniform, top-hat prior PDFs for $f_{\delta, mn} \in [0, f_{\delta, \text{max}}]$,

$$-\sigma_f^2 \ln P_{\text{hat}}(\boldsymbol{\pi}) = \sum_{n, m=1}^{N_z, N_k} \left(f_{\delta, mn}^2 \text{H}[-f_{\delta, mn}] + [f_{\delta, mn} - f_{\delta, \text{max}}]^2 \text{H}[f_{\delta, mn} - f_{\delta, \text{max}}] \right), \quad (27)$$

where $\text{H}(x)$ is the Heaviside step function. Enforcing positive solutions for the matter power spectrum is beneficial in reducing both the statistical errors and oscillations in the reconstruction, as already reported in S12. The positivity priors adopt wide in-

tervals, $f_{\delta, \text{max}} = 100$, compared to expected values of $f_{\delta, mn} \sim 1$. In addition, for numerical convenience, the top-hat priors have soft edges, $\sigma_f = 10^{-2}$, to relax issues with low acceptance rates and undefined gradients in the Monte-Carlo sampler of $P(\boldsymbol{\pi}|\mathbf{d})$ near the edges.

3.4. Monte-Carlo sampler

For sampling the posterior PDF, Eq. (24), we apply a MCMC technique that represents $P(\boldsymbol{\pi}|\mathbf{d})$ by $n_{\text{mcmc}} = 10^4$ points $(\boldsymbol{\pi}_i, w_i)$ with statistical weights, w_i , for given projection parameters \mathbf{q} . The MCMC sampler is a Hamiltonian Monte-Carlo algorithm, known to be efficient even for high-dimensional models ($N_z \times N_k \sim 60$) by proposing new, quickly decorrelating sampling points with high acceptance rate (Gelman et al. 2003). The sampler, however, requires as input the gradient $\nabla_{\boldsymbol{\pi}} \ln \mathcal{L}_q(\mathbf{d}|\boldsymbol{\pi})$ and the gradient of the logarithmic prior densities – all easily available in our case, foremost because of the linear projection $\mathbf{m}(\boldsymbol{\pi}, \mathbf{q}) = \mathbf{X}_q \boldsymbol{\pi} + \boldsymbol{\xi}_q^{\text{fid}}$. We demonstrate the appropriate sampler performance in Appendix A and provide more implementation details there. Due to the efficient decorrelation of the MCMCs, we shorten the burn-in phase for the KiDS-1000 analysis, $n_{\text{burnin}} = 5 \times 10^3$, in comparison to Appendix A, and use shorter chain lengths because of the subsequent merger of many chains when marginalising over \mathbf{q} , outlined in the next section.

3.5. Marginal errors including uncertainties in IA and lensing kernel parameters

The parameters for the lensing kernel and IA are neither exactly known nor intended to be constrained by our shear data. Therefore, to account for their uncertainties in $f_{\delta, mn}$, the analysis combines many chains with $n_{\text{runs}} = 500$ realisations of \mathbf{q} drawn from a baseline error model. The error baseline adopts a flat cosmology, $\Omega_{\Lambda} = 1 - \Omega_m$, and a random sample of the posterior joint distribution of $(\Omega_m, A_{\text{IA}})$ from the recent 3×2 pt cosmological analysis in Heymans et al. (2021); their marginal errors are $\Omega_m = 0.305_{-0.012}^{+0.012}$ and $A_{\text{IA}} = +1.04_{-0.30}^{+0.28}$ (68% CI). The 3×2 pt

experiment combines the KiDS-1000 cosmic shear constraints with those from galaxy-galaxy lensing and, importantly, the galaxy clustering in the partly overlapping, spectroscopic surveys of both the 2-degree Field Lensing Survey and the Baryon Oscillation Spectroscopic Survey (Blake et al. 2016; Alam et al. 2015) to break the $\sigma_8 - \Omega_m$ degeneracy in the shear data. This substantially reduces the uncertainty of Ω_m in the lensing kernel while, at the same time, using only $z \lesssim 1$ data. Furthermore, for error realisations of the source distributions, we shift the histograms in Fig. 1 according to $p_z^{(i)}(z) \rightarrow p_z^{(i)}(z + \delta_z^i)$, for random draws of δ_z^i confined by the error model in Hildebrandt et al. (2021), their Figure 6 and Table 3; the root-mean-square (RMS) error of δ_z^i is $\sigma_z^i \approx 1.3 \times 10^{-2}$ for all tomographic bins, except for $i = 3$ where $\sigma_z^i = 2 \times 10^{-2}$. Within this Monte-Carlo process, the reference $P_\delta^{\text{fid}}(k, z)$ is fixed for all chains to that in Table 1 to avoid conflicting definitions of $f_{\delta, \text{mn}}$ while varying Ω_m .

After all MCMCs with randomised lensing kernels and IA parameters are available, we combine the n_{runs} runs by selecting from each chain j a number of $n_{\text{merge}} = 10^3$ sampling points π_{ij} with probability $w_{ij} / \sum_i w_{ij}$. Selected points are put back into the sample j , to be possibly selected again. By doing so, the selected n_{merge} points sample the posterior of chain j when equally weighted. Mixing the MCMC points from all n_{run} chains for the final Monte-Carlo sample then contains $n_{\text{merge}} \times n_{\text{runs}} = 5 \times 10^5$, equally weighted sampling points π_{ij} of the marginalised posterior distribution of $f_{\delta, \text{mn}}$.

4. Data

We use the public data from the fourth Data Release (DR4) of the Kilo-Degree Survey (Kuijken et al. 2019), commonly referred to as the KiDS-1000 data.¹ The images underlying the data were taken by the high-quality VST-OmegaCAM (Kuijken 2011), covering a total area of about 1006 deg² in four optical filters (*ugri*). After masking, the effective area of the KiDS-1000 data is 777.4 deg². Its overlap with the VIKING survey (Vista Kilo-degree Infrared Galaxy survey, Edge et al. 2013), which observes in five near-infrared bands, *ZYJHK_s*, allows a better control over redshift uncertainties (Hildebrandt et al. 2021).

4.1. Source catalogue

The following summarises the production of the shear catalogue, carried out by the KiDS-1000 Consortium. The images were processed using the THELI (Erben et al. 2005) and ASTRO-WISE (Begeman et al. 2013) pipelines, source ellipticities were estimated by *lensfit* (Miller et al. 2013; Fenech Conti et al. 2017). Based on the nine-band catalogue, individual photometric redshift estimates, z_B , were obtained using BPZ (Benítez 2000), dividing the sources into five tomographic bins (Fig. 1).

To calibrate the redshift distribution of each tomographic bin, Wright et al. (2020a) constructed a self-organising map (SOM) linking the nine-band photometry of the sources to a representative spectroscopic sample. Galaxies without matching spectroscopic counterparts, or for which the z_B are catastrophically different from the redshift of the matched spectroscopic sample, were expunged from the catalogue (Wright et al. 2020b). The mean and the scatter, δ_z^i , on the bias of the means of the $p_z^{(i)}(z)$, estimated by the SOM, were numerically estimated using a suite of KiDS-like mock observations (Hildebrandt et al.

¹ The KiDS data products are public and available through <http://kids.strw.leidenuniv.nl/DR4>

2021).² The resulting ‘gold sample’ contains $\sim 2.1 \times 10^7$ sources with well-calibrated photometric redshift distributions; Giblin et al. (2021) gives more details. Table A.1 in the Appendix summarises the main parameters relevant for our analysis. Cosmological parameter constraints from the KiDS-1000 tomographic data, with the methodology in Joachimi et al. (2021), are presented in Asgari et al. (2021), exclusively using cosmic shear, in Heymans et al. (2021), using 3×2 pt data, and in Tröster et al. (2021), for a beyond Λ CDM analysis using 3×2 pt data.

4.2. Data vector and covariance of measurement noise

Based on the tomographic shear data, the KiDS-1000 DR4 provides estimates of the binned shear correlation function, $\xi_\pm^{(ij)}(\theta)$, for every combination of tomographic bins, (ij) , employing the popular computer software TreeCorr (Jarvis et al. 2004; Jarvis 2015). We use these data without modification. For the ξ_\pm estimator details, we refer the reader to Asgari et al. (2021), Section 2.1 and Appendix C, and only stress that we analyse the $\xi_\pm^{(ij)}(\theta)$ binned into $N_\theta = 9$ angular log-bins for the range $\theta = 0'.5 - 300'$. Another notable technical detail, the data vector for the DR4 was obtained by rebinning a previously finely binned vector, instead of rerunning TreeCorr. Further, Asgari et al. (2021) exclude scales smaller than $4'$ for ξ_- due to high systematic uncertainties in the theoretical matter power-spectrum on very small scales, whereas we include scales down to $0.5'$ for the model-free measurement of $P_\delta(k, z)$.

The covariance matrix of noise, \mathbf{C} in Eq. (25), for the estimator of $\xi_\pm^{(ij)}(\theta)$ uses the analytical model by Joachimi et al. (2021), Appendix E. This model accounts for the intrinsic shape scatter of sources, for both Gaussian and non-Gaussian cosmic variance, mostly relevant towards larger angular scales, for the super-sample covariance due to fluctuation modes greater than the survey footprint, and for the calibration uncertainty in the multiplicative shear bias. Like for $\xi_\pm^{(ij)}(\theta)$, the covariance matrix is part of the package of additional DR4 data products.

4.3. Systematic shear error

In addition to intrinsic alignments, a residual systematic error in the shear signal through the data reduction or the instrument may also be potentially present in $\xi_\pm^{(ij)}$. Negligible when produced by weak gravitational lensing, a detection of *B*-modes in the shear field, this means $\bar{\kappa}(\ell) \neq \bar{\kappa}^*(-\ell)$ in Eq. (2), is considered a sufficient indicator of systematic errors. Clearly separating *B*-modes from *E*-modes in a $\xi_\pm^{(ij)}$ with finite support is, however, unfeasible, but other related statistics are known to separate both modes (and ambiguous modes), most prominently COSEBIs (Schneider et al. 2010). For KiDS-1000, logarithmic COSEBIs capturing scales $\ell \lesssim 10^3$ do not indicate *B*-modes on a 95% confidence level (Asgari et al. 2021; Giblin et al. 2021), several other tests for systematic errors are negative, and the cosmological analysis with the *E*-mode COSEBIs yields results consistent with a $\xi_\pm^{(ij)}$ analysis. Therefore, a significant bias of parameters in a cosmological analysis due to a systematic shear error is unlikely.

Notably, however, the COSEBIs cosmological analysis alone is insensitive to small angular scales of $\ell \sim 10^4$, included in our analysis through $\theta \lesssim 4'$ in $\xi_\pm^{(ij)}$. In addition, even a small systematic shear error in $\xi_\pm^{(ij)}$ might cause artificial deviations of $P_\delta(k, z)$

² Sample variance of the large-scale structure introduces a correlation between the scatter of δ_z^i across different tomographic redshift bins, see Figure 2 in Hildebrandt et al. (2021) for the explicit values.

from the reference $P_{\delta}^{\text{fid}}(k, z)$, i.e., $f_{\delta, mn} \neq 1$, if the error is of the order of the *difference signal* between the measured $\xi_{\pm}^{(ij)}$ and the expected signal in Eq. (14) for $f_{\delta, mn} \equiv 1$. The 1σ – 2σ window left open for *B*-modes by the logarithmic COSEBIs therefore leaves the possibility that deviations in KiDS-1000 might partly be related to a systematic shear error in the data. We return to this caveat in Sect. 6.

5. Results

This section reports our results for the relative power spectrum, $f_{\delta, mn}$, in two variants: an entirely average, non-evolving scenario (one broad redshift bin) and an evolving scenario with three independent redshift bins. In addition, we verify our pipeline with results from a mock analysis based on ray-traced N -body data in an entirely Λ CDM framework.

5.1. Reference Λ CDM matter power-spectrum

For the KiDS-1000 analysis presented here, the reference power spectrum, $P_{\delta}^{\text{fid}}(k, z)$, is a revised *halofit* model with the parameters in Table 1 (Takahashi et al. 2012; Smith et al. 2003). These parameters are maximum-posterior values taken from Table C.1 (3×2 pt, joint) in Heymans et al. (2021) with one modification: the value for σ_8 is lowered from 0.76 to 0.72 to achieve the best-fit to KiDS-1000 data that averages out to $\langle f_{\delta, mn} \rangle_{mn} \approx 1$ over all m and n (the next Sect. 5.2 provides more details). This σ_8 reduction is presumably required because the $P_{\delta}(k, z)$ model in Heymans et al. (2021) includes neutrino suppression and baryonic feedback, missing here, and is, even without neutrinos and baryons, already systematically lower by roughly 5%–10% within $k \approx 0.1$ – $10 h \text{Mpc}^{-1}$ compared to *halofit*. We refer to Section 4 in Mead et al. (2015) for a discussion on the latter aspect, and reiterate that our $P_{\delta}^{\text{fid}}(k, z)$ choice is arbitrary – in our analysis, a purely Λ CDM model that matches the KiDS-1000 data. The results for $f_{\delta}(k, z)$ in the following sections consequently probe the deviations of the true $P_{\delta}(k, z)$ relative to the best-fitting Λ CDM reference.

5.2. Evidence for deviation from reference

A hypothesis test against null models with constant $f_{\delta, mn} = \bar{f}_0$, for all m and n , and fixed projection parameters \mathbf{q} shows that the KiDS-1000 data support deviations from the reference power spectrum in either k or z , shown by the results in Fig. 3. For each \bar{f}_0 on the x -axis in this figure, 10^5 noise realisations of \mathbf{d}_{null} are used in the null model to predict the cumulative distribution $C[t_{\text{null}}]$ of the test statistic $t_{\text{null}} := -2 \ln P(f_{\delta, mn} = \bar{f}_0 | \mathbf{d}_{\text{null}})$. The y -axis shows the probability, $p := C[t_d]$, that the null model exceeds the $t_d := -2 \ln P(f_{\delta, mn} = \bar{f}_0 | \mathbf{d})$ in the actual data (solid line) or, for verification, in random null-model data (dashed line). Starting with the reference power spectrum ($\bar{f}_0 = 1$), as indicated by the yellow vertical line, the KiDS-1000 data have $p = 0.012$ and the verification data $p = 0.78$. Therefore, while the verification data are well within the expectation of the null hypothesis, the KiDS-1000 data are inconsistent with reference model on a $1 - p = 98.8\%$ confidence level. Varying \bar{f}_0 , however, would not improve the test result because the KiDS-1000 curve already peaks at $\bar{f}_0 \approx 1$: the reference power spectrum, $P_{\delta}^{\text{fid}}(k, z)$, is the best fit out of a family of models with constant $f_{\delta, mn}$. The only way to improve the fit would be to make $f_{\delta, mn}$ varying with either scale, k (this means m), or redshift, z (this means n).

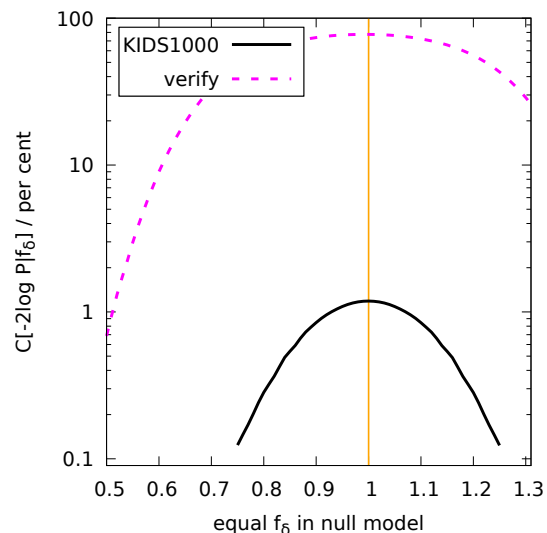


Fig. 3. Test of data against a null model with identical $f_{\delta, mn} = \bar{f}_0$ for all m and n ($N_z = 3$). Shown on the y -axis is the probability of $-2 \ln P(f_{\delta, mn} = \bar{f}_0 | \mathbf{d})$ being greater than in the null model. The dotted line is the result for one noisy verification data vector that has $\bar{f}_0 = 1$; the solid line is for the KiDS-1000 data. The setup in Table 1 and the source distributions in Fig. 1 without errors in the projection parameters are assumed.

In fact, the peak at $\bar{f}_0 \approx 1$ is our deliberate choice for KiDS-1000, achieved by lowering σ_8 for $P_{\delta}^{\text{fid}}(k, z)$ to 0.72 compared to the best-fitting value of 0.78 in Heymans et al. (2021) in order to move the peak from $\bar{f}_0 \approx 0.9$ to its final location $\bar{f}_0 \approx 1$. This way, the $f_{\delta, mn}$ in our data are normalised to the average $\langle f_{\delta, mn} \rangle_{mn} \approx 1$. The failed null test still stands, however, and is evidence for the existence of a better fit by introducing either a k - or z -dependence of $f_{\delta, mn}$, or both. This is explored in the following two more complex scenarios.

5.3. Average deviations over full redshift range

The first scenario introduces a k -dependence for $f_{\delta, mn}$ without redshift evolution ($N_z = 1$), reported with 68% CI about the median in the left panel of Fig. 4. In other words, the redshift evolution of $P_{\delta}(k, z)$ is assumed to be that of the reference power spectrum. Towards nonlinear scales $k \gtrsim 0.1 h \text{Mpc}^{-1}$, there is no indication for a deviation from the reference exceeding the 68% CI, in particular the suppression of power does not fall below $f_{\delta} \approx 0.8$, nor do the data support a boost of power beyond $f_{\delta} \approx 1.2$. Towards linear scales, below $k \approx 0.1 h \text{Mpc}^{-1}$, is a slight, yet insignificant, rise towards $f_{\delta} \approx 1.5$. This might be a sign that *halofit* with higher σ_8 provides a slightly better fit on linear scales. Yet, on average, variations relative to $P_{\delta}^{\text{fid}}(k, z)$ stay within about 20% (68% CI) down to $k \sim 10 h \text{Mpc}^{-1}$.

5.4. Deviations for three separate redshift bins

For more insight in a possible z -evolving f_{δ} in the second scenario, we probe the average $f_{\delta}(k, z)$ inside three separate redshift bins, $Z_1 = [0, 0.3]$, $Z_2 = [0.3, 0.6]$, and $Z_3 = [0.6, 2]$. Their marginalised posterior constraints (68% CI about the median) are plotted as three credible regions in the middle panel of Fig. 4, one region for each redshift bin. The lowest bin, Z_1 ,

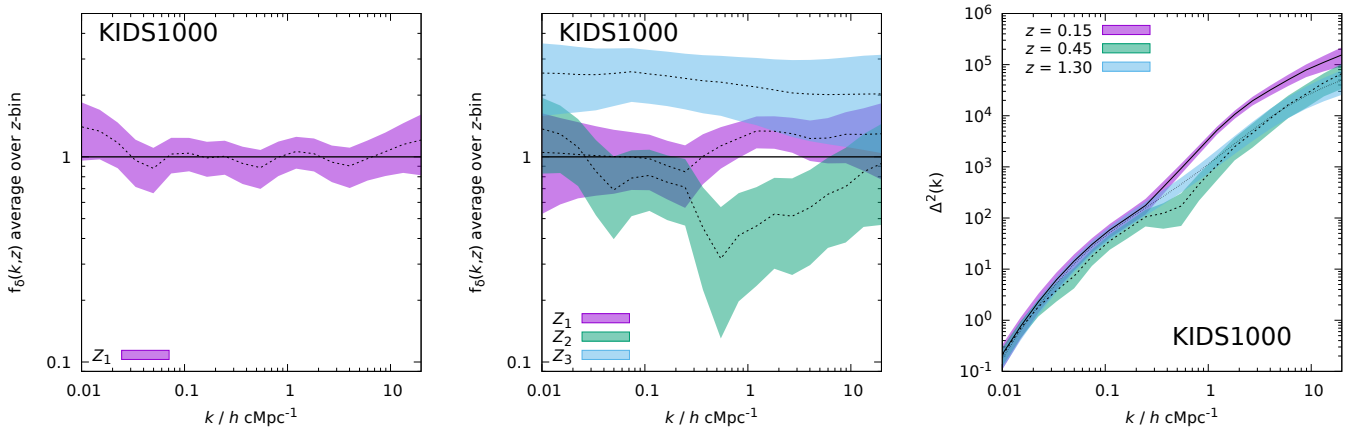


Fig. 4. Reconstructed matter power spectrum in KiDS-1000 for a Tikhonov parameter $\tau = 5.0$ in three variants. Errors marginalise over uncertainties in the lensing kernel and IA. Shown are the posterior 68% CI about the median (lines). *Left panel:* Transfer function $f_\delta(k, z)$ averaged over the entire redshift range $Z_1 = [0, 2]$ and relative to the reference, $P_\delta^{\text{fid}}(k, z)$, with parameters listed in Table 1. *Middle panel:* As the left panel but now for three independent transfer functions averaged separately within the ranges $Z_1 = [0, 0.3]$, $Z_2 = [0.3, 0.6]$, and $Z_3 = [0.6, 2]$. *Right panel:* Dimensionless power spectrum, $\Delta^2(k, z) = 4\pi k^3 P_\delta(k, z) = 4\pi k^3 f_\delta(k, z) P_\delta^{\text{fid}}(k, z)$, interpolated to the centres of three redshift bins Z_1, Z_2 , and Z_3 .

is fully consistent with $f_\delta = 1$, on k -average $f_\delta = 1.15 \pm 0.28$, while the middle bin, Z_2 , on average $f_\delta = 0.57 \pm 0.27$, indicates a power suppression, reaching the depth $f_\delta = 0.3 \pm 0.2$ at $k \sim 0.5 h \text{Mpc}^{-1}$, and the highest bin, Z_3 , overall prefers a boosted power of $f_\delta = 2.22 \pm 0.81$. The signal suppression in the middle redshift bin and the boost in the highest bin cancel each other when averaging f_δ over the whole redshift range, resulting in the $f_\delta = 0.99 \pm 0.20$ in the left panel.

The close description of the $\xi_\pm^{(ij)}(\theta)$ data points by the flexible f_δ model is illustrated by the posterior predictive of the model in Fig. A.6 (Appendix). Shown in the various panels are our KiDS-1000 data points (black with 1σ errors bars) for $\theta \xi_\pm^{(ij)}(\theta)$ (lower left panels) and $\theta \xi_+^{(ij)}(\theta)$ (upper right panels) in comparison to the posterior model constraints (68% and 95% CIs in dark and light blue). The CIs in this plot do not marginalise over \mathbf{q} , which, however, does have a less than 10% affect. The red line corresponds to the Λ CDM reference model, this means $f_{\delta, mn} \equiv 1$, obtained from a best-fit of σ_8 to the data points (Sect. 5.1). Allowing for deviations $f_{\delta, mn} \neq 1$ in the three separate redshift bins Z_1 to Z_3 moves the CIs relative to the reference, thereby improving the fit, although the reference still stays within the 95% CI, as, for instance, for $\xi_\pm^{(55)}(\theta)$. Whilst an overall good match to the (correlated) data points, a conflict with the model is probably present for $\xi_+^{(22)}(\theta)$, and perhaps in $\xi_+^{(12)}(\theta)$ to $\xi_+^{(15)}(\theta)$, where the data prefer a higher amplitude than the model fitting all tomographic bins. Figure A.4 shows a similar plot with verification data, based on the reference model, as comparison. A higher value of $S_8 := \sqrt{\Omega_m}/0.3 \sigma_8 \approx 0.791$, as indicated by the green line for the N -body verification data (without IA, Sect. 5.5), would account for the higher $\xi_+^{(1j)}$ -amplitude but, on the other hand, is rejected by the data due to mismatches at higher redshift (e.g., $\xi_+^{(35)}$ or $\xi_+^{(45)}$). This might indicate spurious systematic errors in the low- z bins, discussed in Sect. 6.

Expressed in terms of the actual power spectrum, $\Delta^2(k, \bar{z}) := 4\pi k^3 f_\delta(k, \bar{z}) P_\delta^{\text{fid}}(k, \bar{z})$, interpolated to the z -bin centres, \bar{z} , the diverse redshift evolution of $f_\delta(k, z)$ in the KiDS-1000 data translates into a suppression of nonlinear structure growth between $0.3 \lesssim z \lesssim 2$. Namely, the $\bar{z} = 0.15$ matter power spectrum in the right panel of Fig. 4 (magenta) has clearly more

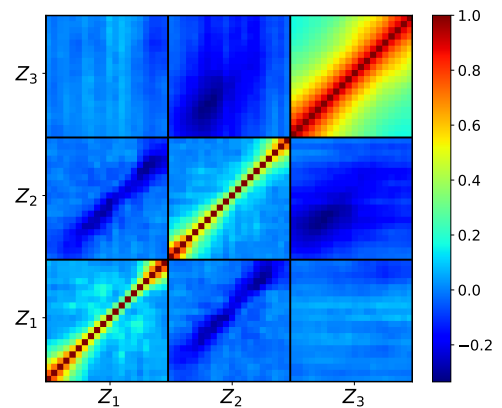


Fig. 5. Correlation matrix of $f_{\delta, mn}$ errors for the KiDS-1000 analysis with three redshift bins, corresponding to the middle and right panels in Fig. 4. The three blocks on the diagonal from bottom left to top right are the correlation matrices for the z -bins $Z_1 = [0, 0.3]$, $Z_2 = [0.3, 0.6]$, $Z_3 = [0.6, 2]$, respectively; off-diagonal blocks show correlations between distinct z -bins; pixels within the 20×20 blocks are correlations between the k -bins, ascending from left to right inside a block.

power than the two higher redshift bins (green for $\bar{z} = 0.45$ and cyan for $\bar{z} = 1.3$) for $k \gtrsim 0.1 h \text{Mpc}^{-1}$, while the two other power spectra are consistent with each other, maybe with the green rising over cyan near $k = 10 h \text{Mpc}^{-1}$. Consequently, with cyan and green being moved closer to each other, there is for $k \gtrsim 0.1 h \text{Mpc}^{-1}$ less structure growth detected between $\bar{z} = 0.45$ – 1.3 than in the reference Λ CDM cosmology but, conversely, more between $\bar{z} = 0.15$ – 0.45 , pulling back the low- z bin to the reference power spectrum.

It is noteworthy that the statistical errors of $f_{\delta, mn}$ and hence $\Delta^2(k, z)$ are correlated, best visualised by the correlation matrix in Fig. 5. Each pixel in the correlation matrix encodes the Pearson correlation coefficient, r , between two k -bins, either from same or from different z -bins. The matrix is organised in $N_k \times N_k$ blocks, where k increases from left to right and top to bottom. The three blocks on the diagonal, bottom left to top right (lowest z to highest z), are correlations within the same redshift bin, and

the six off-diagonal blocks are cross-correlations between distinct z -bins. The enhancement of correlations within the blocks, making them stick out as tiles in a 3×3 mosaic, is a side-effect of the Tikhonov regularisation smoothing the $f_{\delta, mn}$ along the k -axis. Correlations are high for adjacent k -bins in the same z -bin, $r \approx 0.4$ – 0.8 , especially in the highest z -bin (top right), but quickly drop off with distance on the k -scale. Adjacent k -bins are also statistically dependent when from adjacent z -bins, albeit now anti-correlated with typically $r \approx -0.4$ to -0.1 . Not shown is the correlation matrix for a $N_z = 1$ reconstruction, left panel in Fig. 4, to save space; it is essentially a diagonal matrix where adjacent k -bins have $|r| \lesssim 0.1$, except at the lower and upper boundary of the k -range where $r \approx 0.5$ – 0.6 .

5.5. Verification test with ray-traced mock data

To add more realism to the code verification than in Appendix A, especially with respect to the f_{δ} result for $N_z = 3$, we perform a more stringent test with N -body ray-traced data (Takahashi et al. 2017). Like in Burger et al. (2024), we subdivide the 108 full-sky shear fields from the simulated data according to the KiDS-1000 sky area and, for each tomographic bin, combine 30 shear grids for ascending source redshifts according to the redshift distributions in Fig. 1. This yields an ensemble of $n = 1944$ mock KiDS-1000 surveys. From these, source positions are picked to match the angular positions, shear weights, and shape noise to the measured counterparts in the public KiDS-1000 ellipticity catalogue (Giblin et al. 2021). In contrast to Appendix A, however, intrinsic alignments of sources are not included here, thus $A_{\text{IA}} = 0$. Similar to the actual KiDS-1000 data vector, we use TreeCorr to compute $\xi_{\pm}^{(ij)}(\theta)$ from the mock shear catalogues.

Driven first by the question whether our code can recover $f_{\delta}(k, z) = 1$ from a simulated (unrealistically) high S/N data vector when using exactly the same cosmological parameters as in the simulation, we average all n realisations of the data vector, denoted by $\bar{\mathbf{d}}^{\text{sim}}$, and use the individual realisations, $\mathbf{d}_i^{\text{sim}}$, to estimate the (standard) error covariance of $\bar{\mathbf{d}}^{\text{sim}}$,

$$\mathbf{C}^{\text{sim}} = \frac{1}{n(n-1)} \sum_{i=1}^n (\mathbf{d}_i^{\text{sim}} - \bar{\mathbf{d}}^{\text{sim}})(\mathbf{d}_i^{\text{sim}} - \bar{\mathbf{d}}^{\text{sim}})^{\text{T}}. \quad (28)$$

This covariance matrix is turned into an unbiased estimator of the inverse covariance using Hartlap et al. (2007). The average $\bar{\mathbf{d}}^{\text{sim}}$ and \mathbf{C}^{sim} are basically a single measurement in a hypothetical survey with n times the angular area than KiDS-1000, albeit underestimating the cosmic variance error. For an initial inspection, the solid green lines SIM-THS17 in Fig. A.6 (Appendix) compares $\bar{\mathbf{d}}^{\text{sim}}$ to the real KiDS-1000 data (black data points with error bars): The simulated tomography correlations are mostly within the 1σ noise scatter of the KiDS-1000 data points, yet exhibit systematically more signal compared to the reference model (red lines) by occasionally exceeding the 95% CIs, probably due to the higher fluctuation amplitude, $S_8 \approx 0.791$ in the simulation compared to $S_8 \approx 0.765$ in KiDS-1000, and, less relevantly, the missing IA terms in the simulation. Now, using $\bar{\mathbf{d}}^{\text{sim}}$ and \mathbf{C}^{sim} as input, the data points in the top panel of Fig. 6 show the code results for $f_{\delta}(k, z)$ in three redshift bins. To test the code's ability to recover the power spectrum in the simulation, $f_{\delta}(k, z) = 1$, the reference $P_{\delta}^{\text{fid}}(k, z)$ is set here to the same cosmological parameters as in the N -body data, namely $\Omega_{\text{m}} = 0.279$, $\Omega_{\Lambda} = 1 - \Omega_{\text{m}}$, $\Omega_{\text{b}} = 0.046$, $h = 0.7$, $n_{\text{s}} = 0.97$, and $\sigma_8 = 0.82$. Since the lensing kernel is exactly known in this experiment, no marginalisation of \mathbf{q} is done. We find the following.

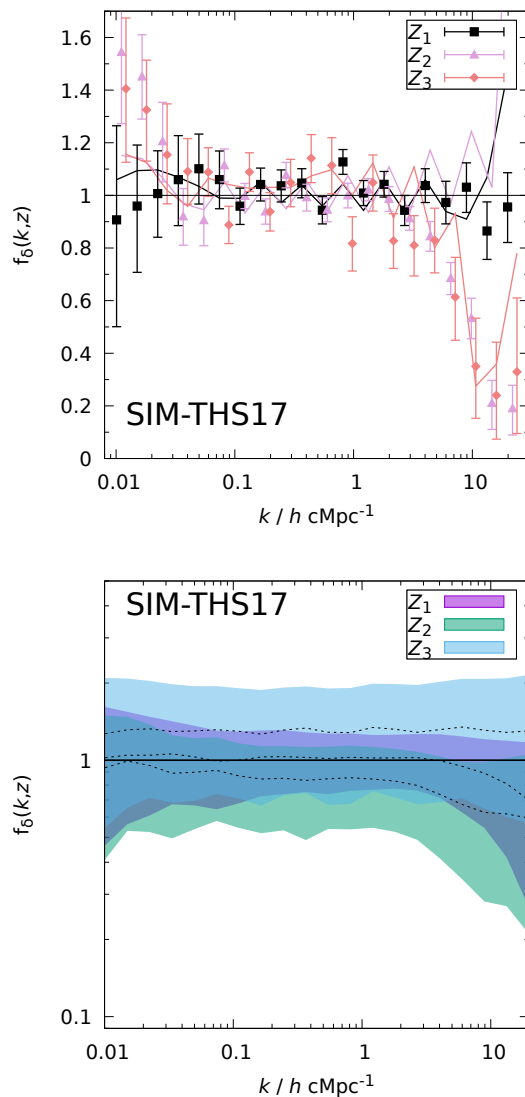


Fig. 6. Verification test of the analysis code for $f_{\delta}(k, z)$ using: a N -body simulated data vector, averaged over $n = 1944$ realisations of the KiDS-1000 data without IA; the code and data setup for the KiDS-1000 analysis with three redshift bins $Z_1 = [0, 0.3]$, $Z_2 = [0.3, 0.6]$, and $Z_3 = [0.6, 2]$. The reference power, $P_{\delta}^{\text{fid}}(k, z)$, is here identical to the cosmology of the simulation (Takahashi et al. 2017). The errors (68% CI) do not marginalise over a projection kernel uncertainty. *Top panel:* For the simulated covariance of the average data, comprising n times the area of KiDS-1000. Deviations from the expected $f_{\delta}(k, z) = 1$ towards higher z and $k \gtrsim 1 h \text{ Mpc}^{-1}$ are related to the finite grid pixel size in the simulation (pixelation bias). The lines are additional reconstructions using noise-free data, based on Eq. (8) and `halofit` without pixelation bias. *Bottom panel:* Now with statistical errors as in a single KiDS-1000 survey.

The reconstructed power spectrum in Fig. 6, top panel, for the lowest redshift bin (filled squares) is overall consistent with $f_{\delta, mn} = 1$ for the range $k = 0.01$ – $20 h \text{ Mpc}^{-1}$ within the 68% CI, indicated by the error bars. But two significant deviations emerge: first, in the higher redshift bins beyond $k \approx 5 h \text{ Mpc}^{-1}$, and, second, smaller deviations around $0.01 h \text{ Mpc}^{-1}$. The high- k suppression of the signal is a real feature in the simulation data due to the pixelated shear grids of the simulation (pixel size $0''.4$), significantly biasing low the values for $\xi_{-}^{(ij)}$ for $\theta \lesssim 5'$. The low-

est redshift bin is presumably also affected, but scales of a few arcmins correspond here to a characteristic k too high to be visible in the plot: the typical wave number, $k_{\text{eff}} = 2\pi/(f_{\kappa}(\chi_d)\theta_{l'})$, of an angular scale $\theta_{l'} = 1'$ on a lens plane at distance χ_d corresponds to $k_{\text{eff}} \approx 33.5, 12.0, 5.2 h \text{Mpc}^{-1}$ for lens planes located at the centres of the bins Z_1 , Z_2 , and Z_3 , respectively. The additional lines in the plot support the idea of a pixelation bias: they are reconstructions of noise-free data, based on the simple Limber-Kaiser projection in Eq. (8) – crucially, not showing the systematic signal drop for Z_2 , or for Z_3 around $k = 1 h \text{Mpc}^{-1}$. Instead, however, the lines exhibit artefacts as zig-zag oscillations of amplitude $\Delta f_{\delta} \approx 0.1$, strongly increasing towards the edges of the plotted k -range and probably related to the limitations of the deprojection method (Sect. 3.1). The artefacts are partly mirrored in the data point scatter and overlap with the pixelation bias for Z_3 (yet not for Z_2) at large k .

The second, weaker $\sim 1.5\sigma$ – 2σ deviations appear around $k = 0.01 h \text{Mpc}^{-1}$ for Z_2 and Z_3 . They, too, are probably to some extent present in the N -body data: Figure 19 in Takahashi et al. (2017) report a 10% deviation from halofit near $k = 0.01 h \text{Mpc}^{-1}$. Nevertheless, we doubt that this explains the full effect and point out that the plots compare an average data vector in a simulation of finite volume, still subject to noise, to the cosmic average. Especially on large scales, cosmic variance noise is relevant and under-estimated in \mathbf{C}^{sim} . In addition, the noise-free data (solid lines) suggest some excess signal on large scales due to edge artefacts. In summary, the bottom panel of Fig. 6 is an excellent reconstruction of the relative power with $\Delta f_{\delta} \approx 0.1$ accuracy, or better, for $k \lesssim 10 h \text{Mpc}^{-1}$ and $z \lesssim 1$.

Another inference of $f_{\delta}(k, z)$ with the simulated data is shown in the bottom panel of Fig. 6 – this time for a KiDS-1000-like error covariance, $n \times \mathbf{C}^{\text{sim}}$. By using the average \bar{d}^{sim} as input, the (essentially linear) reconstruction in the figure represents the ensemble mean of $f_{\delta}(k, z)$ posteriors in three redshift bins. In this average reconstruction, the posterior errors are similar to the ones in the KiDS-1000 reconstruction, middle panel of Fig. 4, increasing in size for higher z , although now the $f_{\delta, \text{mm}}$ are consistent with $f_{\delta} = 1$ throughout (68% CI). The suppression of power by pixelation bias is here fully contained within the statistical errors, only vaguely hinted at in the green Z_2 posterior region of Fig. 6, bottom panel, which falls just below $f_{\delta} = 1$ around $k = 10 h \text{Mpc}^{-1}$. Therefore, also for KiDS-1000-like noise levels, the code recovers the correct power spectrum in the N -body data. The highest precision of $f_{\delta} = 1.00 \pm 0.27$ is achieved for Z_1 , the middle bin Z_2 has $f_{\delta} = 0.81 \pm 0.31$, and Z_3 $f_{\delta} = 1.29 \pm 0.63$ (medians and 68% CIs, no \mathbf{q} errors).

For comparison, Fig. A.5 in the Appendix shows an ensemble of reconstructions with individual, 16 randomly chosen $\mathbf{d}_i^{\text{sim}}$, illustrating the possible variations in the inferred $f_{\delta}(k, z)$. Each panel is a prediction of a KiDS-1000 reconstruction in a Λ CDM scenario. Here, we observe a small tendency of the posterior median in Z_3 to be above $f_{\delta} = 1$ and the median in Z_2 to be below $f_{\delta} = 1$, despite both having $f_{\delta} \approx 1$ for $k \lesssim 5 h \text{Mpc}^{-1}$. This tendency is also visible in Fig. 6 of average reconstructions, bottom panel, with the posterior median always being above $f_{\delta} = 1$ for Z_3 , or below for Z_2 , and probably has two reasons. First, the Z_3 bin is poorly constrained, giving a broad marginalised posterior PDF skewed towards higher f_{δ} values, shifting up the centres (posterior medians) of our CIs; this is illustrated by Fig. A.3. Second, errors in Z_2 and Z_3 are anti-correlated, preferring a lower value for Z_2 , if the f_{δ} at similar k in Z_3 is scattered upwards. But, on a broad note, one should not expect the maximum of the marginalised PDF to coincide with the maximum of

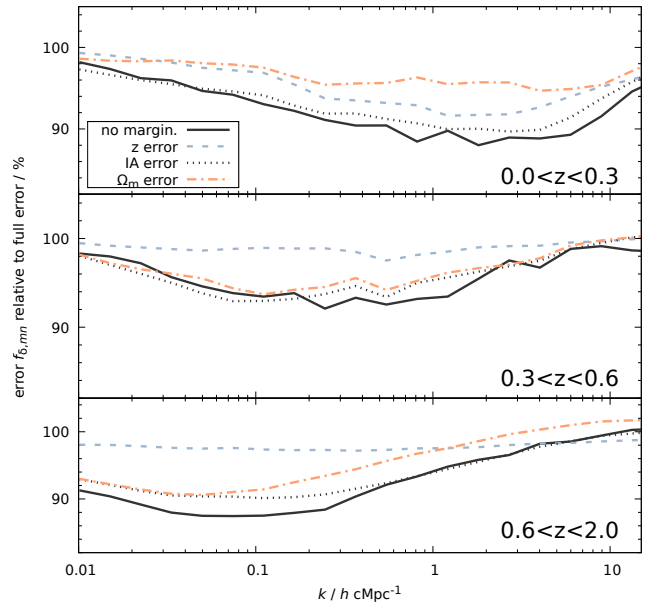


Fig. 7. Percentage fraction in total marginal posterior error of $f_{\delta, \text{mm}}$ due to uncertainties in the lensing kernel and IA parameter. Shown is the statistical error relative to the full marginal error (RMS variance of posterior) as function of k in three redshift bins without marginalisation (solid lines), with marginalisation over errors in the source redshift distributions only (dashed lines), Ω_m in the lensing kernel only (dashed-dotted lines), and for the A_{IA} error only (dotted lines).

the full posterior (for the non-marginalised parameters) because this requires the full posterior PDF to obey certain symmetries about its maximum, as, for instance, present in a multivariate Gaussian posterior – excluded here because of our skewed, non-Gaussian marginalised posterior distributions. For increased S/N in the data, however, the long tails of skewed posteriors are suppressed, and the median shift is no longer discernible in the top panel of Fig. 6.

5.6. Impact of uncertainty in IA and lensing kernel

The individual impact by uncertainties in the projection parameters \mathbf{q} on the reconstructed $f_{\delta, \text{mm}}$ is of interest for improving future analyses or to gauge the relevance of errors in the projection kernel. We therefore compare the marginalised $f_{\delta, \text{mm}}$ errors in the middle panel of Fig. 4 to the statistical errors obtained without marginalisation, or to the errors where all parameters \mathbf{q} are fixed but for one that is marginalised over.

Figure 7 shows the results in these different scenarios as function of scale k for three z -bins, indicated in the lower right of each panel; a 100% error is as large as in a scenario where all \mathbf{q} uncertainties are marginalised over. The solid black lines use a fixed \mathbf{q} without any marginalisation, setting a lower limit for all scenarios (but is also subject to numerical noise owing to the limited number of realisations, $n_{\text{merge}} = 500$). A lower limit of 90% to the black line for all k means that uncertainties due to source shape noise, cosmic variance, and calibrated shear bias, all accounted for in the noise covariance \mathbf{C} , are responsible for at least 90% of the total error in the reconstruction, while the addition of lensing kernel uncertainties and IA errors amounts to 10% or less of the total. This addition is explored in more detail by the dashed lines that marginalise over redshift errors only, the dotted-dashed lines for only Ω_m uncertainties in the lensing ker-

nel, and the dotted lines for A_{IA} errors only. In summary, IA errors have a subdominant impact, about several per cent, reflected by the closeness of the dotted line to the solid line. The largest impact of the Ω_m uncertainty is in the lowest z -bin, whereas the uncertainty in the source z -distributions is the dominating contributor in the middle and highest z -bin for $k \lesssim 1 h \text{Mpc}^{-1}$. Therefore, better calibrating photo- z errors in future analyses yields improvements of up to 10% in the total statistical error.

6. Discussion

This study presents, verifies, and applies to KiDS-1000 data a revised method for reconstructing the three-dimensional (band) matter power-spectrum with tomographic shear data. Our approach relies on the specification of a projection kernel only and is hence agnostic about an analytical model for $P_\delta(k, z)$ while being applicable for all cosmologies where the $\xi_\pm^{(ij)}(\theta)$ are projections of $P_\delta(k, z)$ along the line of sight. Numerically convenient, we express $P_\delta(k, z) =: f_\delta(k, z) P_\delta^{\text{fid}}(k, z)$ in terms of a reference and probe deviations, $f_{\delta, mn} \in [0, 100]$, relative to it, putting the free variables $f_{\delta, mn}$ into the same dynamical range. Not required, however, is a reference close to the true power spectrum: for instance, Fig. 2 uses a reference fixed in cosmic time, to highlight the structure growth, or, on the extreme end, a constant $P_\delta^{\text{fid}}(k, z) \equiv P_0$ would yield a $f_{\delta, mn}$ that directly represents the power spectrum. Nor does rescaling $P_\delta^{\text{fid}}(k, z)$ by a constant inside any z -bin, whilst redefining $f_{\delta, mn}$, affect the inferred $\Delta^2(k, z) \propto f_\delta(k, z) P_\delta^{\text{fid}}(k, z)$: the reconstructed matter power spectrum is robust against the reference used. Choosing a reference towards a slowly evolving $f_\delta(k, z)$ is nevertheless preferable because the z -bin-average that the $f_{\delta, mn}$ represent depends on the specific noise properties and source z -distributions in the tomographic survey – a comparison to theoretical models will have to replicate the data-specific z -weighting more closely for a significantly varying $f_\delta(k, z)$ inside a wide z -bin. This is obvious in Fig. 2 for a z -independent reference where more weight is given closer to the lower boundary of each z -bin: the average $f_{\delta, mn}$ is close to the true $f_\delta(k, z)$ near $z_{\text{max}} = 0.13, 0.4, 0.7$ for Z_1, Z_2 , and Z_3 ; yet the bin centres are at $z_{\text{mid}} = 0.15, 0.45, 1.30$. For our analysis, we use as reference a best-fitting ΛCDM model without baryonic feedback or neutrinos. Although being a good fit to the data already, as shown by the red lines relative to the black data points in Fig. A.6, the $f_{\delta, mn}$ indicate where additional changes might be needed, or how much deviation from the reference is acceptable until we conflict with the data. We proceed here with two variants of the analysis, one for an $f_{\delta, mn}$ -average over the full redshift range and one to probe the z -evolution of $f_\delta(k, z)$.

Our first variant in the left panel of Fig. 4 averages $f_\delta(k, z)$, denoted $\bar{f}_\delta(k)$ hereafter, over the entire z -range covered by KiDS-1000, with most signal from essentially $z \lesssim 1$. This analysis shows that in the nonlinear regime, $k \approx 0.05\text{--}10 h \text{Mpc}^{-1}$, the KiDS-1000 matter power-spectrum is consistent with the ΛCDM reference in Table 1 within 20% (68% CI). Therefore, there is no evidence for a variation, suppression or boost, exceeding 20% relative to the reference scenario with purely cold dark matter. This is also within the range reported by other lensing studies, discussed below, although we caution that the results are not always one-to-one comparable to ours because they are partly based on the premise that the lensing $P_\delta(k, z)$ has the $Planck S_8$ (Planck Collaboration et al. 2020) but is attenuated in the nonlinear regime to fit the lensing measurements of significantly lower S_8 to explain the “ S_8 tension”. Such an attenuation, if present, would be addressed in our reference by a systematic

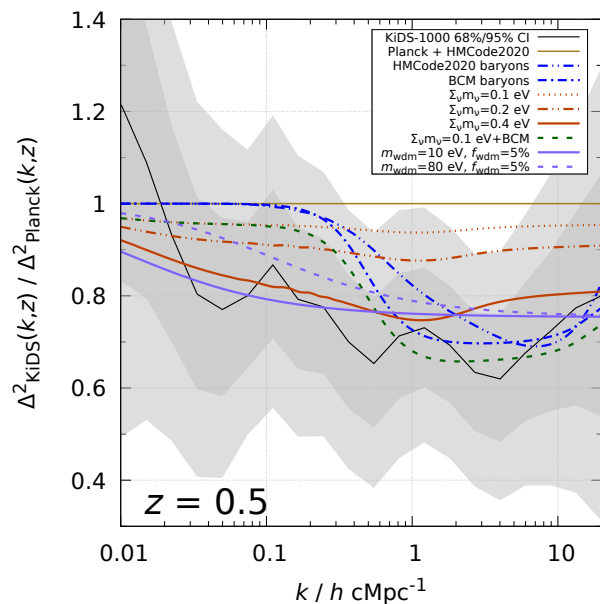


Fig. 8. Power spectrum ratio $\Delta_{\text{KiDS}}^2(k, z)/\Delta_{\text{Planck}}^2(k, z)$ at $z = 0.5$. Shown in grey are the 68% and 95% CI from our analysis. The KiDS-1000 spectrum $\Delta_{\text{KiDS}}^2(k, z)$ uses the $f_{\delta, mn}$ in Fig. 4 averaged within one broad redshift bin (left panel). The $Planck$ model for $\Delta_{\text{Planck}}^2(k, z)$ is the TT, TE, EE+lowE best-fit of a standard ΛCDM (Planck Collaboration et al. 2020) extrapolated to $z = 0.5$ with HMCCode2020 by Mead et al. (2021). The lines are model transfer functions to $\Delta_{\text{Planck}}^2(k, z)$ invoking flavours of strong baryonic feedback (HMCCode2020: $\log_{10}(T_{\text{AGN}}/\text{K}) = 8.8$, $A_{\text{baryon}} = 3.13$, $\eta_{\text{baryon}} = 0.603$; BCM by Schneider & Teyssier 2015: $\log_{10}(M_c/h^{-1}M_\odot) = 15.0792$, $\eta_b = 0.5$, $k_s = 55.0$), neutrino suppression for cumulative neutrino masses Σ_ν, m_ν (BCM), or a mixture of CDM and WDM (Kamada et al. 2016, m_{wdm} : WDM particle mass, f_{wdm} : WDM mass fraction).

cally lower S_8 instead of fully showing up in $\bar{f}_\delta(k)$ – especially because our data lack constraining power in the unattenuated, linear regime, $k \lesssim 0.01 h \text{Mpc}^{-1}$. To level the field with analyses using the $Planck S_8$ as premise, we change the reference to a power spectrum with $Planck$ cosmology, $\Delta_{\text{Planck}}^2(k, z)$, and recast Fig. 4, left panel, into Fig. 8 for the ratio $\Delta^2(k, \bar{z})/\Delta_{\text{Planck}}^2(k, \bar{z})$ at $\bar{z} = 0.5$, a redshift where the lensing method is roughly most sensitive. Only from this $Planck$ perspective, our results now clearly require a suppression, $1 - f_{\delta, mn}$, of the ΛCDM reference at $k \approx 3 h \text{Mpc}^{-1}$ of up to $35\% \pm 15\% \pm 25\%$ (68% and 95% CI). As indicated by lines in the plot, it is conceivable to explain the tension with $Planck$ by a variety of hypothetical mechanisms involving, among others, strong baryonic feedback, (sterile) neutrinos, or alternatives to non-interacting cold dark-matter.

Therefore, whereas a CDM power spectrum without suppression and low S_8 is on average a good description of the KiDS-1000 shear tomography, small modifications to CDM would be insufficient to reconcile KiDS-1000 with $Planck$: mechanisms with a substantial, more than 20% suppression, have to be invoked – in agreement with other recent studies analysing KiDS-1000 lensing data. For instance, the recent Schneider et al. (2022, S+22) combines KiDS-1000 data with observations of X-ray emission and the kinematic Sunyaev–Zeldovich (kSZ) effect in galaxy clusters to inform baryonic feedback parameters incorporated in their ΛCDM -flavoured $P_\delta(k, z)$. By initially using KiDS-1000 data alone, the deviations from their model without baryonic feedback are inconclusive but stay, as in our measurement in

left panel of Fig. 4, within 10–20% for $k = 1\text{--}10 h \text{Mpc}^{-1}$ (68% CI). Only when adding the X-ray and kSZ data, their constraints strongly favour a power suppression of up to 30% (68% CI) at $k \approx 5 h \text{Mpc}^{-1}$, somewhat more than our data support. Building only on lensing information, Preston et al. (2023, PEG23) analyse KiDS-1000 and data from the third-year Dark Energy Survey (DES Y3) to extend a Λ CDM model by one modification parameter, A_{mod} , pushing the nonlinear $P_{\delta}(k, z)$, equivalent to $A_{\text{mod}} = 1$, towards the linear power spectrum, $A_{\text{mod}} = 0$. Their KiDS-1000 fit with uninformative priors on cosmological parameters and $A_{\text{mod}} \in [-5, 5]$ is – like in Fig. 4 – inconclusive, $A_{\text{mod}} \approx 0.9 \pm 0.2$ (their Figure 2, left panel). However, when assuming a *Planck* cosmology and the suppression-inclined prior $A_{\text{mod}} \in [0.5, 1]$, PEG23 claim strong evidence for a suppression of $\approx 25\% \pm 6\%$ at $k \approx 3 h \text{Mpc}^{-1}$ (68% CI), more significant yet fully consistent with our Fig. 8 (we reiterate our relaxed prior $f_{\delta, mn} \in [0, 10^2]$). Furthermore, Broxterman & Kuijken (2024, BK24) fit a double power-law $P_{\delta}(k, z) \propto k^p (1+z)^{-mbk}$ to $\xi_{\pm}^{(ij)}(\theta)$ for KiDS-1000, DES Y3, and the third year Hyper Suprime-Cam Survey (HSC Y3), yielding a reasonable Λ CDM match without suppression in the range $k = 0.01\text{--}5 h \text{Mpc}^{-1}$ (68% CI) and a 2σ agreement among the three stage-III surveys. Compared to our results for $N_z = 1$, similarly averaging over the full redshift range, their constraints are weaker in the nonlinear regime ($f_{\delta} \approx 0.8^{+0.5}_{-0.2}$), despite the same data, probably because of our tighter Ω_m prior for the projection kernel: the $P_{\delta}(k, z)$ amplitude in $\xi_{\pm}^{(ij)}(\theta)$ is degenerate with the pre-factor Ω_m^2 in the Eqs. (8)–(10). Finally, similar results are reported by authors that use only DES Y3 lensing data although the required suppression in the nonlinear regime relative to *Planck* tends to be somewhat lower than for KiDS-1000 by a factor between one and two (Bigwood et al. 2024, PEG23, Ferreira et al. 2024, Aricò et al. 2023). In conclusion, other works support our finding of an average matter power spectrum that at $k \gtrsim 0.05 h \text{Mpc}^{-1}$ is either within 20% tolerance a purely Λ CDM spectrum of low $S_8 \approx 0.73$, or a spectrum with both higher *Planck* $S_8 \approx 0.83$ and significant suppression of up to 20%–30% in the nonlinear regime relative to CDM.

Surprisingly, our KiDS-1000 analysis becomes more complex and discrepant with our best-fitting Λ CDM reference of low S_8 if the $f_{\delta, mn}$, unlike in previous studies, are freed to vary with redshift, achieved in our second analysis by increasing the number of z -bins to $N_z = 3$ broad z -bins. This is only practical by employing Tikhonov regularisation, or something else to this effect, as clearly illustrated by the dramatically shrinking sizes of the credible regions from $\tau = 0$ to $\tau = 5$ in Fig. 2. Applied to KiDS-1000, the 68% CI constraints in the middle panel of Fig. 4 then depict a remarkably diverse picture: only the $f_{\delta, mn}$ in the low- z bin, $Z_1 = [0, 0.3]$, are now consistent with the reference matter-power spectrum, averaged for all k -bins to $\bar{f}_{\delta} = 1.15 \pm 0.28$, whereas the power spectrum in $Z_2 = [0.3, 0.6]$ is overall suppressed, $\bar{f}_{\delta} = 0.57 \pm 0.27$, and boosted for $Z_3 = [0.6, 2]$ where $\bar{f}_{\delta} = 2.22 \pm 0.81$. The verification tests in Appendix A, for analytic data (noisy) vectors, and in Sect. 5.5, for mock N -body shear catalogues, assure us of an $f_{\delta, mn}$ accuracy of 10% or better within $k \approx 0.01\text{--}10 h \text{Mpc}^{-1}$. The noticed tendency of shifting the median posterior $f_{\delta, mn}$ of our 68% CIs towards $\bar{f}_{\delta} \approx 1.3$ for Z_3 and towards $\bar{f}_{\delta} \approx 0.8\text{--}0.9$ for Z_2 , due to the broadened skewed posterior PDFs in these z -bins, actually goes into the direction of the KiDS-1000 result. It is nevertheless too small for the pronounced split between Z_2 and Z_3 credible regions in the real data which also are, unlike the verification results, blurred by the IA and lensing kernel uncertainties (an extra $\sim 10\%$ error, Fig. 7). In fact, for the baseline $f_{\delta}(k, z) \equiv 1$ in Fig. A.5, the split in the

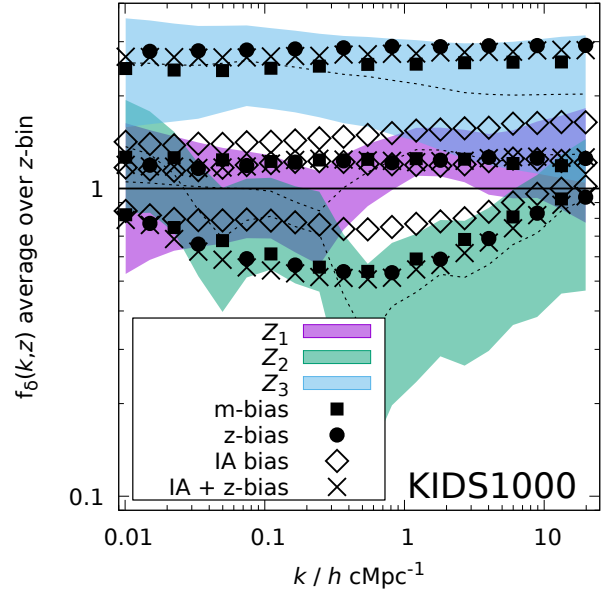


Fig. 9. KiDS-1000 results for $f_{\delta, mn}$, as in middle panel of Fig. 4, in relation to alternative hypotheses using the reference cosmology $P_{\delta}^{\text{fid}}(k, z)$ and best-fitting bias parameters to match the KiDS-1000 data vector, $\xi_{\pm}^{(ij)}(\theta)$: Filled squares assume shear m -bias factors $\{m_i\} = \{+1.00, +0.48, -0.023, -0.028, +0.035\}$, filled circles assume photo- z biases $\{\delta_z^i\} = \{-0.075, -0.079, +0.009, +0.018, -0.052\}$, and open diamonds employ the eNLA model with $\{A'_{\text{IA}}, z_{\text{piv}}, \eta\} = \{0.3, 0.19, 1.5\}$. Crosses assume a hybrid model of eNLA and a smaller z -bias: $\{A'_{\text{IA}}, z_{\text{piv}}, \eta\} = \{0.45, 0.25, 2.3\}$ and $\{\delta_z^i\} = \{-0.017, -0.058, +0.027, +0.025, -0.043\}$. The data points indicate the posterior median (CIs are similar to that of the shaded regions), filled data points use alternating k -bins to avoid overlap.

mock data realisations is not nearly as pronounced as for KiDS-1000, making the KiDS-1000 result very roughly a $1/16 \approx 6\%$ event, or less, for the baseline scenario.

To explore the possibility of spurious systematic errors possibly mimicking the evolving $f_{\delta}(k, z)$, we estimate in three scenarios the amplitude of bias needed to replicate our KiDS-1000 results if the Λ CDM reference were the true matter power spectrum. First, a spurious shear m -bias in the data shall be the dominating source of systematic error. The required bias is then obtained through fitting $(1+m_i)(1+m_j)\xi_{\pm}^{(ij), \text{fid}}(\theta)$, predicted by the reference model, to the KiDS-1000 data vector by maximising the data likelihood, Eq. (25), with respect to the bias parameters m_i in the tomographic bins i . The corresponding (posterior median) $f_{\delta, mn}$ of the best-fitting model are plotted as data points with filled squares in Fig. 9 in comparison to KiDS-1000 (shaded regions). Evidently, the m -bias model closely traces the KiDS-1000 results, but, according to its best-fit parameters $\{m_i\} = \{+1.00, +0.48, -0.023, -0.028, +0.035\}$, needs an unrealistic m -bias in the first two source bins that exceeds the reported values in Asgari et al. (2021) by more than 30σ . The second scenario assumes spurious photo- z errors in $p_z^{(i)}(z)$ as dominating source of bias. Again, we fit a $\xi_{\pm}^{(ij), \text{fid}}(\theta)$ to the KiDS-1000 data vector, now for the $p_z^{(i)}(z + \delta_z^i)$ shifted by the bias parameters δ_z^i , while the reconstruction uses the original $p_z^{(i)}(z)$. The best-fit values are $\{\delta_z^i\} = \{-0.075, -0.079, +0.009, +0.018, -0.052\}$. Like in the previous m -bias scenario, this model equally well fits

the KiDS-1000 results, filled circles in Fig. 9, but requires a high bias (photo- z s are systematically low) in the first two and the last source z -bins. This bias level exceeds the estimated tolerances of photo- z errors in the KiDS-1000 gold sample by more than 5σ (Table A.1). A third conceivable source of systematic error is an IA model bias. Too simplistic physically, the approximations in the NLA model are nevertheless flexible enough to fit measurements of IA as a means for calibrating the IA distortion of $\xi_{\pm}^{(ij)}(\theta)$ (Fortuna et al. 2021; Preston et al. 2024). It may be, however, that z -binning of $\Delta^2(k, z)$ makes us sensitive to a z -dependent IA amplitude, missing in the NLA model and typically irrelevant in stage-III cosmological analyses. To test if a z -dependent IA amplitude $A_{IA}(z) := A'_{IA} (1+z)^\eta (1+z_{\text{piv}})^{-\eta}$, as in the eNLA model, potentially explains the $f_{\delta, mn}$ data after all, we fit $\xi_{\pm}^{(ij), \text{fid}}(\theta)$ to KiDS-1000 by varying $\{A'_{IA}, z_{\text{piv}}, \eta\}$ only, yielding the parameters $\{0.3, 0.19, 1.5\}$ for the open diamond data points in Fig. 9. Crucially, the reconstruction algorithm is ignorant about $A_{IA}(z)$ and assumes a constant A_{IA} . Indeed, then some of the split between Z_2 and Z_3 (especially the drop in Z_2) could be explained by the IA model bias. And, since $z_{\text{piv}} = 0.3$ and $\eta = 1.5$ are deemed consistent with KiDS-1000 uncertainties in Asgari et al. (2021), this hypothesis is a plausible explanation for at least part of the \bar{f}_{δ} redshift variation. More plausible even is a combination of $A_{IA}(z)$ and a moderate photo- z bias, 2σ – 4σ , indicated by the crosses in Fig. 9. Lastly, recalling the 1σ – 2σ evidence for B -modes in Sect. 4.3, a systematic shear error might also be relevant here. But, lacking a KiDS-1000 model of these for $\xi_{\pm}^{(ij)}$, it is unclear if they plausibly contribute to the $\bar{f}_{\delta} \neq 1$ result. In summary, whereas (especially) m -biases and photo- z biases alone are unlikely sources of systematic errors that shape the result of evolving \bar{f}_{δ} , the negligence of a z -dependent IA amplitude, A_{IA} , as in our reconstruction setup, in combination with moderate photo- z biases might explain our $N_z = 3$ result. At this point, we are unable to exclude either possibility, or that of small systematic errors related to B -modes, but stress that the discussed scenarios mainly target the first two tomographic bins, $z_B \leq 0.5$, where the posterior predictive of the model also indicates some conflict with the data (Fig. A.6). Future reconstructions of the matter power spectrum inside separate redshift bins should also pay close attention to the IA modelling in the analysis.

A truly evolving $f_{\delta}(k, z)$, on the other hand, would offer insights into the physics of nonlinear structure growth at $k \gtrsim 0.1 h \text{Mpc}^{-1}$ and $z \lesssim 1$. In brief, the KiDS-1000 data indicate too little power for the epoch $z \approx 0.3$ – 0.6 and too much power for $z \approx 0.6$ – 2 , compared to the purely- Λ CDM reference model that actually matches the $f_{\delta, mn}$ averaged in a single z -bin (68% CI). Phrasing this a bit more carefully, this statement applies to weighted averages inside three wide z -bins where most weight is given to $\Delta^2(k, z)$ around $z \approx 0.13, 0.4, 0.7$ for Z_1, Z_2 , and Z_3 , similar to Fig. 2. Still, the average deviations in the Z_2 and Z_3 are, in fact, such that they make $\Delta^2(k, z)$ inside the bins statistically consistent (right panel of Fig. 4), independent of the chosen reference – thus there is no significant detection of any growth from about $z = 0.7$ to 0.4 . The only increase in power is detected towards lower $z \approx 0.13$. This qualitatively matches the S_8 -tension: cosmological probes that give more weight to $z \gtrsim 0.7$, such as CMB experiments, would observe a $\Delta^2(k, z)$ with amplitude higher than in our reference, hence a higher S_8 , whereas probes more sensitive to $z \sim 0.4$ or lower, such as lensing experiments, would observe a $\Delta^2(k, z)$ with S_8 equal to our reference or even lower. We are not aware of a similar conclusion in the lensing literature, although the recent BK24 report a vanishing growth rate at 1σ , their growth index m_{BK} , for KiDS-1000

and HSC Y3 (yet not for DES Y3). That finding for m_{BK} might be related to our result, depending on how the Z_1 – Z_3 are effectively weighted in the BK24 analysis. Possible physical causes of the peculiar structure growth in KiDS-1000 compared to the reference model are, however, presumably nontrivial and beyond the scope of this paper. For example, a baryonic feedback model would have to be strongly evolving with redshift below $z \sim 1$ (and non-monotonic) to match the KiDS-1000 $f_{\delta, mn}$, typically not found in state-of-the-art models (e.g., Schaller et al. 2024, and references therein).

Finally, the close connection of the S_8 -tension to the KiDS-1000 result for $\Delta^2(k, z)$ in $N_z = 3$ z -bins makes this an interesting case, either as evidence in favour of modifications towards the structure growth in the Λ CDM reference, or in favour of spurious systematic errors in a shear tomography analysis mimicking the tension. This evidence appears to be unnoticed in previous stage-III analyses – a full analytic model of $\Delta^2(k, z)$ fitted to the shear tomography can give an unsuspecting match like our $N_z = 1$ analysis – so that a confirmation of the KiDS-1000 result with other lensing data is important. Furthermore, looking forward not too far into the future, stage-IV data will be available soon with roughly 20 times the survey area of KiDS-1000 and also deeper observations, with surveys such as the space-based missions *Euclid* and *Roman*, or the ground-based survey by *Rubin*. Of these the *Euclid* Wide Survey will provide tomographic measurements within 13 source z -bins up to $z \sim 2.5$, statistical errors reduced by about one order of magnitude compared to stage-III, and an excellent control of systematic errors for shear and photo- z . We see no restriction for applying our reconstruction technique to stage-IV data, merely assuming a lensing kernel and an (possibly updated and carefully calibrated) IA model. This promises measurements of the matter power spectrum at different redshift to unprecedented precision, maybe up to $z \sim 2$ with $N_z = 4$ or more bins, critically testing models of the nonlinear structure growth.

Acknowledgements. This paper went through the KiDS review process. We also want to thank Jeger Broxtermann for useful comments. LP acknowledges support from the DLR grant 50QE2002. PB acknowledges financial support from the Canadian Space Agency (Grant No. 23EXPROSS1) and the Waterloo Centre for Astrophysics. Some results in this paper are based on observations made with ESO Telescopes at the La Silla Paranal Observatory under programme IDs 177.A-3016, 177.A-3017, 177.A-3018 and 179.A-2004, and on data products produced by the KiDS consortium. The KiDS production team acknowledges support from: Deutsche Forschungsgemeinschaft, ERC, NOVA and NWO-M grants; Target; the University of Padova, and the University Federico II (Naples).

References

- Abbott, T. M. C., Abdalla, F. B., Alarcon, A., et al. 2018, *Phys. Rev. D*, 98, 043526
- Alam, S., Albareti, F. D., Allende Prieto, C., et al. 2015, *ApJS*, 219, 12
- Aricò, G., Angulo, R. E., Zennaro, M., et al. 2023, *A&A*, 678, A109
- Asgari, M., Lin, C.-A., Joachimi, B., et al. 2021, *A&A*, 645, A104
- Bacon, D. J., Taylor, A. N., Brown, M. L., et al. 2005, *MNRAS*, 363, 723
- Bartelmann, M. & Schneider, P. 2001, *Phys. Rep.*, 340, 291
- Begeman, K., Belikov, A. N., Boxhoorn, D. R., & Valentijn, E. A. 2013, *Experimental Astronomy*, 35, 1
- Benítez, N. 2000, *ApJ*, 536, 571
- Bigwood, L., Amon, A., Schneider, A., et al. 2024, *MNRAS*, 534, 655
- Blake, C., Amon, A., Childress, M., et al. 2016, *MNRAS*, 462, 4240
- Bridle, S. & King, L. 2007, *New Journal of Physics*, 9, 444
- Brooks, S., Gelman, A., Jones, G., & Meng, X. 2011, *Handbook of Markov Chain Monte Carlo*, Chapman & Hall/CRC Handbooks of Modern Statistical Methods (CRC Press)
- Broxterman, J. C. & Kuijken, K. 2024, *A&A*, 692, A201
- Bucko, J., Giri, S. K., Peters, F. H., & Schneider, A. 2024, *A&A*, 683, A152
- Burger, P. A., Porth, L., Heydenreich, S., et al. 2024, *A&A*, 683, A103
- Crittenden, R. G., Natarajan, P., Pen, U.-L., & Theuns, T. 2001, *ApJ*, 559, 552

- Croft, R. A. C. & Metzler, C. A. 2000, *ApJ*, 545, 561
- Edge, A., Sutherland, W., Kuijken, K., et al. 2013, *The Messenger*, 154, 32
- Erben, T., Schirmer, M., Dietrich, J. P., et al. 2005, *Astronomische Nachrichten*, 326, 432
- Euclid Collaboration: Mellier, Y., Abdurro'uf, Acevedo Barroso, J. A., et al. 2024, arXiv:2405.13491
- Fenech Conti, I., Herbonnet, R., Hoekstra, H., et al. 2017, *MNRAS*, 467, 1627
- Ferreira, T., Alonso, D., Garcia-Garcia, C., & Chisari, N. E. 2024, *Phys. Rev. Lett.*, 133, 051001
- Fortuna, M. C., Hoekstra, H., Joachimi, B., et al. 2021, *MNRAS*, 501, 2983
- García-García, C., Zennaro, M., Aricò, G., Alonso, D., & Angulo, R. E. 2024, *JCAP*, 2024, 024
- Gelman, A., Carlin, J., Stern, H., & Rubin, D. 2003, *Bayesian Data Analysis*, Chapman & Hall/CRC Texts in Statistical Science (Chapman & Hall/CRC)
- Gelman, A. & Rubin, D. B. 1992, *Statistical Science*, 7, 457
- Giblin, B., Heymans, C., Asgari, M., et al. 2021, *A&A*, 645, A105
- Harnois-Déraps, J., Martinet, N., & Reischke, R. 2022, *MNRAS*, 509, 3868
- Harnois-Déraps, J., van Waerbeke, L., Viola, M., & Heymans, C. 2015, *MNRAS*, 450, 1212
- Hartlap, J., Simon, P., & Schneider, P. 2007, *A&A*, 464, 399
- Heymans, C., Grocutt, E., Heavens, A., et al. 2013, *MNRAS*, 432, 2433
- Heymans, C., Tröster, T., Asgari, M., et al. 2021, *A&A*, 646, A140
- Hilbert, S., Hartlap, J., White, S. D. M., & Schneider, P. 2009, *A&A*, 499, 31
- Hildebrandt, H., van den Busch, J. L., Wright, A. H., et al. 2021, *A&A*, 647, A124
- Hinshaw, G., Larson, D., Komatsu, E., et al. 2013, *ApJS*, 208, 19
- Hirata, C. M. & Seljak, U. 2004, *Phys. Rev. D*, 70, 063526
- Hu, W. & Keeton, C. R. 2002, *Phys. Rev. D*, 66, 063506
- Jarvis, M. 2015, *TreeCorr: Two-point correlation functions*, Astrophysics Source Code Library, record ascl:1508.007
- Jarvis, M., Bernstein, G., & Jain, B. 2004, *MNRAS*, 352, 338
- Jing, Y. P., Zhang, P., Lin, W. P., Gao, L., & Springel, V. 2006, *ApJ*, 640, L119
- Joachimi, B., Lin, C. A., Asgari, M., et al. 2021, *A&A*, 646, A129
- Joachimi, B., Mandelbaum, R., Abdalla, F. B., & Bridle, S. L. 2011, *A&A*, 527, A26
- Joachimi, B. & Schneider, P. 2008, *A&A*, 488, 829
- Kaiser, N. 1992, *ApJ*, 388, 272
- Kamada, A., Inoue, K. T., & Takahashi, T. 2016, *Phys. Rev. D*, 94, 023522
- Kilbinger, M. 2015, *Reports on Progress in Physics*, 78, 086901
- Kilbinger, M., Heymans, C., Asgari, M., et al. 2017, *MNRAS*, 472, 2126
- Kuijken, K. 2011, *The Messenger*, 146, 8
- Kuijken, K., Heymans, C., Dvornik, A., et al. 2019, *A&A*, 625, A2
- Kuijken, K., Heymans, C., Hildebrandt, H., et al. 2015, *MNRAS*, 454, 3500
- Laguë, A., Schwabe, B., Hložek, R., Marsh, D. J. E., & Rogers, K. K. 2024, *Phys. Rev. D*, 109, 043507
- Lamman, C., Tsaprazi, E., Shi, J., et al. 2024, *The Open Journal of Astrophysics*, 7, 14
- Li, X., Zhang, T., Sugiyama, S., et al. 2023, *Phys. Rev. D*, 108, 123518
- Mauland, R., Winther, H. A., & Ruan, C.-Z. 2024, *A&A*, 685, A156
- Mead, A. J., Brieden, S., Tröster, T., & Heymans, C. 2021, *MNRAS*, 502, 1401
- Mead, A. J., Peacock, J. A., Heymans, C., Joudaki, S., & Heavens, A. F. 2015, *MNRAS*, 454, 1958
- Mezzetti, M., Bonometto, S. A., Casarini, L., & Murante, G. 2012, *JCAP*, 2012, 005
- Miller, L., Heymans, C., Kitching, T. D., et al. 2013, *MNRAS*, 429, 2858
- Murata, K. & Takeuchi, T. T. 2022, *PASJ*, 74, 1329
- Pen, U.-L., Lu, T., van Waerbeke, L., & Mellier, Y. 2003, *MNRAS*, 346, 994
- Planck Collaboration, Aghanim, N., Akrami, Y., et al. 2020, *A&A*, 641, A6
- Pranjal R., S., Krause, E., Dolag, K., et al. 2024, arXiv:2410.21980
- Preston, C., Amon, A., & Efstathiou, G. 2023, *MNRAS*, 525, 5554
- Preston, C., Amon, A., & Efstathiou, G. 2024, *MNRAS*, 533, 621
- Salcido, J., McCarthy, I. G., Kwan, J., Upadhye, A., & Font, A. S. 2023, *MNRAS*, 523, 2247
- Schaller, M., Schaye, J., Kugel, R., Broxterman, J. C., & van Daalen, M. P. 2024, arXiv:2410.17109
- Schneider, A., Giri, S. K., Amodeo, S., & Refregier, A. 2022, *MNRAS*, 514, 3802
- Schneider, A. & Teyssier, R. 2015, *JCAP*, 2015, 049
- Schneider, P. 2006, in *Saas-Fee Advanced Course 33: Gravitational Lensing: Strong, Weak and Micro*, ed. G. Meylan, P. Jetzer, P. North, P. Schneider, C. S. Kochanek, & J. Wambsganss, 269–451
- Schneider, P., Eifler, T., & Krause, E. 2010, *A&A*, 520, A116
- Schneider, P., van Waerbeke, L., Kilbinger, M., & Mellier, Y. 2002, *A&A*, 396, 1
- Secco, L. F., Samuroff, S., Krause, E., et al. 2022, *Phys. Rev. D*, 105, 023515
- Seljak, U. 1998, *ApJ*, 506, 64
- Simon, P. 2012, *A&A*, 543, A2
- Simon, P. & Hilbert, S. 2018, *A&A*, 613, A15
- Smith, R. E. & Markovic, K. 2011, *Phys. Rev. D*, 84, 063507
- Smith, R. E., Peacock, J. A., Jenkins, A., et al. 2003, *MNRAS*, 341, 1311
- Spergel, D., Gehrels, N., Baltay, C., et al. 2015, arXiv:1503.03757
- Sugiyama, N. 1995, *ApJS*, 100, 281
- Takahashi, R., Hamana, T., Shirasaki, M., et al. 2017, *ApJ*, 850, 24
- Takahashi, R., Sato, M., Nishimichi, T., Taruya, A., & Oguri, M. 2012, *ApJ*, 761, 152
- Tegmark, M. & Zaldarriaga, M. 2002, *Phys. Rev. D*, 66, 103508
- The LSST Dark Energy Science Collaboration, Mandelbaum, R., Eifler, T., et al. 2018, arXiv:1809.01669
- Tröster, T., Asgari, M., Blake, C., et al. 2021, *A&A*, 649, A88
- Truttero, O., Zuntz, J., Poursidou, A., & Robertson, N. 2024, arXiv:2410.18191
- Wright, A. H., Hildebrandt, H., van den Busch, J. L., & Heymans, C. 2020a, *A&A*, 637, A100
- Wright, A. H., Hildebrandt, H., van den Busch, J. L., et al. 2020b, *A&A*, 640, L14
- Ye, G., Jiang, J.-Q., & Silvestri, A. 2024, arXiv:2411.07082
- Yoshida, H. 1990, *Physics Letters A*, 150, 262

Appendix A: Hamiltonian Monte-Carlo algorithm

The Bayesian reconstruction of the 3D matter power spectrum, expressed by $\boldsymbol{\pi} = (\dots, f_{\delta,mm}, \dots)$, is numerically challenging due to the high number of variables, up to $N_z \times N_k = 60$ or more in future stage-IV applications. As practical solution, the following describes our implementation details of a Hamiltonian Monte-Carlo sampler of the posterior PDF $P(\boldsymbol{\pi}|\mathbf{d})$, as well as our verification and convergence tests. Compared to a Metropolis-Hastings algorithm, this MCMC approach has an improved convergence and quicker decorrelation – but requires first-order derivatives of the posterior PDF. The derivatives are here easily obtained analytically, contrary to previous KiDS-1000 cosmology analyses where other MCMC algorithms were used. We focus on the specifics of our implementation but refer to Brooks et al. (2011) for more background information.

Appendix A.1: Basic concept

In brief, the Hamiltonian MCMC algorithm is based on the insight from statistical mechanics that a canonical ensemble of particles $j = 1 \dots N_z \times N_k$ with generalised coordinates π_j , masses m_j , canonical moments p_j , the Hamiltonian

$$H(\boldsymbol{\pi}, \mathbf{p}) = U(\boldsymbol{\pi}) + \sum_j \frac{p_j^2}{2m_j}, \quad (\text{A.1})$$

and temperature parameter β randomly occupies states in phase space according to the PDF

$$\begin{aligned} f(\boldsymbol{\pi}, \mathbf{p}) &= \frac{1}{Z} \exp(-\beta H[\boldsymbol{\pi}, \mathbf{p}]) \\ &= \frac{1}{Z} \exp(-\beta U[\boldsymbol{\pi}]) \exp\left(-\beta \sum_j \frac{p_j^2}{2m_j}\right), \end{aligned} \quad (\text{A.2})$$

where the partition function, Z , is a normalisation constant. Turning this insight around, our sampler simulates a canonical ensemble following individual particles along trajectories under the influence of the potential $U(\boldsymbol{\pi}) = -\ln P(\boldsymbol{\pi}|\mathbf{d})$ to trace the posterior PDF, $P(\boldsymbol{\pi}|\mathbf{d})$. The trajectory of each particle is determined by the symplectic Hamilton equations

$$\begin{aligned} \frac{d\pi_j}{dt} &= + \frac{\partial H(\boldsymbol{\pi}, \mathbf{p})}{\partial p_j} = \frac{\beta p_j}{m_j}; \\ \frac{dp_j}{dt} &= - \frac{\partial H(\boldsymbol{\pi}, \mathbf{p})}{\partial \pi_j} = -\beta \frac{\partial U(\boldsymbol{\pi})}{\partial \pi_j}, \end{aligned} \quad (\text{A.3})$$

interrupted by random jumps between hyper-planes of constant energy, $E(\boldsymbol{\pi}, \mathbf{p}) = H(\boldsymbol{\pi}, \mathbf{p}) = \text{const}$, such that energy levels change from E to E' with probability $\min\{1, e^{\beta(E-E')}\}$. These random events simulate the transfer of energy between particles and a heat bath of temperature $T \propto \beta^{-1}$. Ignoring the moments p_j , the distribution of states $\boldsymbol{\pi}_i$ of an ensemble of particles then samples the marginalised PDF

$$\int_{V_p} d\mathbf{p} f(\boldsymbol{\pi}, \mathbf{p}) \propto \exp(-\beta U[\boldsymbol{\pi}]) = [P(\boldsymbol{\pi}|\mathbf{d})]^\beta. \quad (\text{A.4})$$

This does not mean, however, moments can be chosen arbitrarily. Instead, the p_j obey the Gaussian distribution of a maximum-entropy ensemble in $f(\boldsymbol{\pi}, \mathbf{p})$ and, therefore, are randomly set to $p_j \sim \mathcal{N}(0, \sigma_p)$, where $\sigma_p^2 = m_j/\beta$, in the algorithm below. For convenience, we set the heat bath temperature to $\beta \equiv 1$, thus the ensemble $\boldsymbol{\pi}_i$ samples the posterior $P(\boldsymbol{\pi}|\mathbf{d})$, as needed.

Appendix A.2: Implementation details

The art of optimising the Hamiltonian MCMC is in the way we evolve states in the canonical ensemble, how we switch between energy levels, which sampling points are kept, and how particle masses, m_j , are chosen. For our application, we found sufficient convergence already when using a simplistic model of equal mass weights, $m_j \equiv 1$. Furthermore, to produce a sequence of sampling points $\boldsymbol{\pi}_i$, we follow the MCMC standard procedure.

1. We pick a random starting point, $\boldsymbol{\pi}$, $i = 0$.
2. The elements of the momentum in \mathbf{p} , conjugate to $\boldsymbol{\pi}$, are randomised independently, $p_j \sim \mathcal{N}(0, \sigma_p)$.
3. The algorithm then numerically integrates the Hamilton Eqs. (A.3) with a symplectic integrator to follow the trajectory, starting from $(\boldsymbol{\pi}, \mathbf{p})$, for n equal time steps Δt , proposing the end point as a new MCMC point, $(\boldsymbol{\pi}_{n\Delta t}, \mathbf{p}_{n\Delta t})$.
4. This proposal $\boldsymbol{\pi}_{n\Delta t}$ is accepted with probability $\min\{1, e^{\beta(E-E_{n\Delta t})}\}$, where $E := H(\boldsymbol{\pi}, \mathbf{p})$ and $E_{n\Delta t} := H(\boldsymbol{\pi}_{n\Delta t}, \mathbf{p}_{n\Delta t})$ are the energies of the initial and the proposed new state. If rejected, we go back to the initial trajectory point, $\boldsymbol{\pi}$, and start again from step 2.
5. If accepted, we keep the proposed state as MCMC data point, $\boldsymbol{\pi}_i = \boldsymbol{\pi}_{n\Delta t}$. Since rejections mean we have to go back and reuse a sampling point, the stored $\boldsymbol{\pi}_i$ has weight $w_i = 1 + n_{r,i}$, where $n_{r,i}$ denotes the number of rejections needed for $\boldsymbol{\pi}_i$.
6. We stop after n_{mcmc} accepted sampling points $(\boldsymbol{\pi}_i, w_i)$, or start over again from step 2 with $\boldsymbol{\pi} = \boldsymbol{\pi}_i$ and $i \rightarrow i + 1$ otherwise.

In contrast to Metropolis-Hastings, the Hamiltonian method proposes a new MCMC point by (approximately) transporting the previous point along the iso-contours of the posterior density, keeping the rejection rate low even if the previous and proposed point are well separated, thereby decorrelating sampling points. Notably, this way of proposing new points is symmetric due to the time symmetry of the Hamilton equations and the isotropy of the randomised momenta, satisfying the conditions of a detailed balance. In addition, as long as the time symmetry is preserved, unavoidable inaccuracies when numerically integrating Eqs. (A.3) do not bias the sampling, although they usually increase rejection rates when moving too far away from the posterior density iso-contours. As discussed in Brooks et al. (2011), the leapfrog method is a suitable choice as numerical integrator of (A.3) for a MCMC sampler due to its symplectic symmetry. To increase the acceptance rate for larger time steps Δt , we use the more accurate 4th-order, also symplectic, integrator. The various integrator steps are not spelt out here in detail to save space but can be found in Yoshida (1990).

To control the rejection rate of the MCMC sampler, we adjust the size of a time step, Δt . Decreasing the time step, Δt , typically lowers the rejection rate, but boosts correlations between the sampling points. Starting from $\Delta t = 10^{-3}$, we follow the heuristic to keep the rejection rate somewhere around 30% by (i) decreasing $\Delta t \rightarrow \frac{\Delta t}{1.2}$, if the rate exceeds 50%, or (ii) by increasing $\Delta t \rightarrow 1.2 \Delta t$, if it falls below 16%, after 20 consecutive accepted sampling points. At the same time, the number of trajectory steps is fixed to $n = 100$. With these settings, the time steps stabilise typically around $\Delta t = 10^{-2}$. As final data product, we keep $n_{\text{mcmc}} = 5 \times 10^4$ sampling points after a burn-in phase of 2×10^4 steps during which the step size is continuously adjusted. For all chains, we start the burn-in with the initial state drawn from a normal distribution centred around $f_{\delta,mm} = 1$, $f_{\delta,mm} \sim \mathcal{N}(1, 0.5)$.

To compute the movement along a trajectory by the Hamilton equations, we employ an analytic expression for the gradient

$$\nabla_{\pi} U(\boldsymbol{\pi}) = -\nabla_{\pi} \ln \mathcal{L}_q(\mathbf{d}|\boldsymbol{\pi}) - \nabla_{\pi} \ln P_{\text{hat}}(\boldsymbol{\pi}) - \nabla_{\pi} \ln P_{\tau}(\boldsymbol{\pi}) \quad (\text{A.5})$$

which, for Eq. (24), is split into three summands: one for the likelihood,

$$-\nabla_{\pi} \ln \mathcal{L}_q(\mathbf{d}|\boldsymbol{\pi}) = (\mathbf{C}^{-1} \mathbf{X}_q)^{\text{T}} (\mathbf{X}_q \boldsymbol{\pi} + \boldsymbol{\xi}_q^{\text{fid}} - \mathbf{d}), \quad (\text{A.6})$$

one for the top-hat priors,

$$\frac{\partial \ln P_{\text{hat}}(\boldsymbol{\pi})}{\partial f_{\delta, mn}} = \begin{cases} 2\sigma_f^{-2} f_{\delta, mn} & , \text{if } f_{\delta, mn} \leq 0 \\ 2\sigma_f^{-2} (f_{\delta, mn} - f_{\delta, \text{max}}) & , \text{if } f_{\delta, mn} > f_{\delta, \text{max}} \end{cases}, \quad (\text{A.7})$$

and one for the Tikhonov regularisation,

$$\frac{\partial \ln P_{\tau}(\boldsymbol{\pi})}{\partial f_{\delta, mn}} = \begin{cases} 2\tau (f_{\delta, 1n} - f_{\delta, 2n}) & , \text{if } m = 1 \\ 2\tau (f_{\delta, N_k n} - f_{\delta, (N_k - 1)n}) & , \text{if } m = N_k \\ 2\tau (2f_{\delta, mn} - f_{\delta, (m-1)n} - f_{\delta, (m+1)n}) & , \text{if } 1 < m < N_k \end{cases}. \quad (\text{A.8})$$

The computation time of the sampler can be reduced by computing the matrix $(\mathbf{C}^{-1} \mathbf{X}_q)^{\text{T}}$ just once and then reusing it for fixed projection parameters \mathbf{q} .

Appendix A.3: Verification and convergence tests

To validate the convergence of the Monte-Carlo sampler, we carry out three different tests using the KiDS-1000 data vector for the projection parameters \mathbf{q} as in Table 1. The setup is identical to that in our analysis in Sect. 5.4 for the most complex model with three redshift bins, $N_z = 3$. The first test is a sanity check to verify by eye the transition towards a stationary process during the burn-in phase. For this, we inspect as function of iteration i the variation of $f_{\delta, mn}$ and the (negative log-) probability $-2 \ln P(\boldsymbol{\pi}|\mathbf{d})$ along the chain. The top panel of Fig. A.1 is one random example; other chains and variables $f_{\delta, mn}$ in $\boldsymbol{\pi}_i$ look qualitatively similar and are not shown here. Apart from the deep drop of $-2 \ln P$ at the very beginning of the chain, where the sampler takes the points away from the initial random $\boldsymbol{\pi}$, there are no more systematic drifts present for $f_{\delta, mn}$ and $-2 \ln P$. This indicates a stationary sampling is quickly reached.

The second test, bottom panel of Fig. A.1, quantifies the decorrelation of sampling points, $\boldsymbol{\pi}_i$, along the chain. For a fair sampling of the posterior density, the sampling points have to become independent quickly. To quantify this, we look at the correlation coefficients $R_{mn, kl}$ in the covariance matrix $\langle \boldsymbol{\pi}_i \boldsymbol{\pi}_{i+\delta i}^{\text{T}} \rangle$ of two sampling points $\boldsymbol{\pi}_i = (\dots, f_{\delta, mn}, \dots)$ and $\boldsymbol{\pi}_{i+\delta i} = (\dots, f_{\delta, kl}, \dots)$ separated by a lag of δi iterations along the same chain. The expectation is that the amplitude of $R_{mn, kl}$ between a pair of model coefficients $f_{\delta, mn}$ and $f_{\delta, kl}$ decreases towards zero with increasing lag δi . This is indeed the case, as shown in the figure bottom panel for several independent chain runs. The orange curves report for a series of ten MCMCs the trend of the maximum $|R_{mn, kl}|$ for all coefficient combinations (m, n) and (k, l) , the blue curves are the average of all $|R_{mn, kl}|$. All chains exhibit the same trend: the maximum $|R_{mn, kl}|$ quickly falls below a few per cent

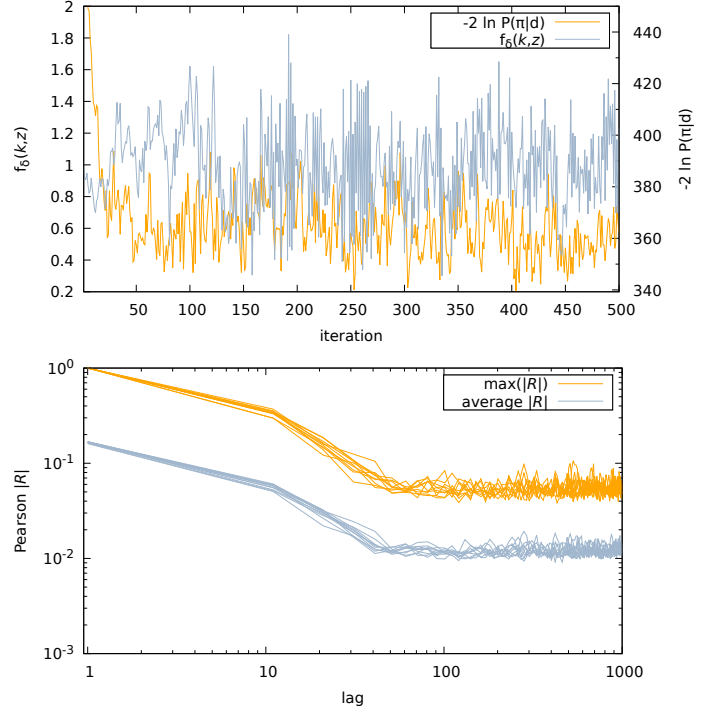


Fig. A.1. Diagnostic plots of the Hamiltonian MCMC sampler with KiDS-1000 data and our final analysis setup for fixed projection parameters as in Table 1. *Top panel:* Example of $f_{\delta, mn}$ variations along one random chain at the beginning of the burn-in, starting from the random initial point $i = 0$ (blue line). The orange line depicts the (negative log-) posterior probability $-2 \ln P(\boldsymbol{\pi}|\mathbf{d})$. *Bottom panel:* Decrease of the correlation of $f_{\delta, mn}$ and $f_{\delta, kl}$ with δi iterations lag as estimated in ten randomly chosen, independent chains. The orange lines follows, one line per chain, the maximum absolute-value Pearson correlation coefficient $|R_{mn, kl}|$, while the blue lines follows the average $|R_{mn, kl}|$ over all variable combinations (mn, kl) . The sampling points quickly decorrelate after a few hundred iterations; the flattening after lag $\delta i \sim 100$ is due to the statistical error in the estimated $|R|$ for chains of finite length $n_{\text{mcmc}} = 5 \times 10^4$.

already after $\delta i \sim 100$, whereas the average $|R_{mn, kl}|$ is even lower, reaching sub-percent levels. After that, all curves tend to flat out, probably due to statistical noise in our $|R_{mn, kl}|$ estimates from the finite number of pairs of sampling points in a given chain.

For the third convergence check, we apply the Gelman–Rubin diagnostics to all coefficients $f_{\delta, mn}$ individually (Gelman & Rubin 1992). This test probes if a single chain has sufficiently converged, by comparing our $n_{\text{chain}} = 10$ independent MCMC runs. Similar to the marginalisation process, Sect. 3.5, we are not using the full chains but, instead, randomly draw $n_{\text{merge}} = 10^3$ points for a thinned each chain. The Gelman–Rubin statistic $t_{\text{gr}} := \sqrt{\hat{V}/W}$ is based on the average $\bar{f}_{\delta, mnk}$ and variance of $\sigma_{\delta, mnk}^2$ of $f_{\delta, mn}$ within a (thinned) chain k , where $W := \sum_k \sigma_{\delta, mnk}^2 / n_{\text{chain}}$ is the average of all within-chain variances, $B/n_{\text{merge}} := \sum_k (\bar{f}_{\delta, mnk} - \bar{f}_{\delta, mn})^2 / (n_{\text{chain}} - 1)$ for $\bar{f}_{\delta, mn} := \sum_k \bar{f}_{\delta, mnk} / n_{\text{chain}}$ is the variance between chains, and $\hat{V} := \frac{n_{\text{merge}} - 1}{n_{\text{merge}}} W + \frac{n_{\text{chain}} + 1}{n_{\text{chain}}} B / n_{\text{merge}}$. The ratio B/W follows a F -distribution in the null hypothesis of independent, stationary chains, and normally distributed $f_{\delta, mn}$; and $t_{\text{gr}} \sim 1$ is to high confidence $t_{\text{gr}} < 1.1$. We repeatedly find $t_{\text{gr}} < 1.001$ for all our free model variables, $f_{\delta, mn}$, consistent with the null hypothesis.

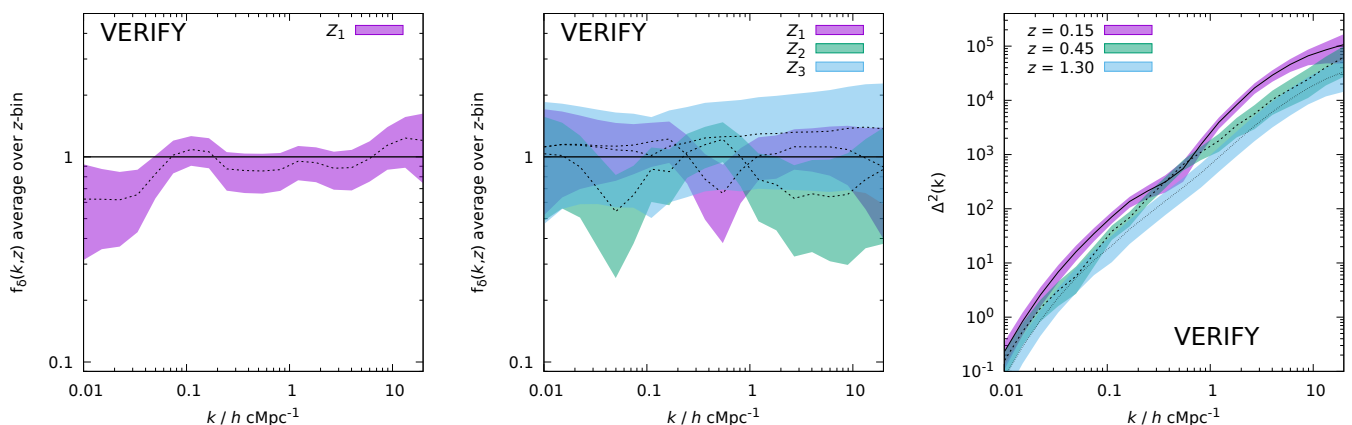


Fig. A.2. Reconstructed relative power spectrum, $f_{\delta}(k, z)$, in redshift range $0 \leq z < 2$ using a verification data vector mimicking KiDS-1000 data (noise added, not marginalising IA or lensing kernel errors). The true relative power has $f_{\delta} \equiv 1$ for all scales and redshift. The data vector is computed from an independent code, not based on the projection matrix $X^{(ij)}(\theta; m, n)$. Shown is the posterior median within a 68% CI. The reconstructions use a Tikhonov parameter of $\tau = 5.0$. *Left panel:* The relative power is averaged over the entire redshift range $Z_1 = [0, 2]$. *Middle panel:* For a relative power that is averaged independently for three redshift bins $Z_1 = [0, 0.3]$, $Z_2 = [0.3, 0.6]$, and $Z_3 = [0.6, 2]$. *Right panel:* Dimensionless average power spectrum, $\Delta^2(k, z) = 4\pi k^3 P_{\delta}^{\text{hd}}(k, z) f_{\delta}(k, z)$, interpolated to the centres of the redshift bins Z_1 to Z_3 .

For test reconstructions of the 3D matter power spectrum, Fig. A.2 shows two successful verification runs of the sampler, but now with simulated data, a model correlation vector, \mathbf{d} , with added random noise according to the Gaussian likelihood model of the KiDS-1000 data. The verification data assume a matter power spectrum identical to $P_{\delta}^{\text{hd}}(k, z)$, thus $f_{\delta, mn} = 1$ for all m and n . In order to not rely on our MCMC code and the $X_{\pm}^{(ij)}(\theta; m, n)$ expansion in particular, we calculate the verification data vector $\xi_{\pm}^{(ij)}(\theta)$, Eq. (7), with a separate computer code from a past study (Simon & Hilbert 2018). The left panel in Fig. A.2, plots the results for $f_{\delta, mn}$ averaged over one redshift bin, $N_z = 1$. The middle panel, uses another noise realisation and splits, as before, $f_{\delta, mn}$ into $N_z = 3$ broad redshift bins to probe the z -evolution. In both panels, we find results consistent with the true values $f_{\delta, mn} = 1$ on a 68% CI level.

Increasing the number of z -bins decreases the constraining power for each bin. This adds skewness to the posterior PDF of $f_{\delta, mn}$, especially for Z_3 , as illustrated by Fig. A.3. The figure shows the posterior PDF of $f_{\delta, mn}$ in three z -bins at fixed comoving scale $k = 1.8 h \text{ Mpc}^{-1}$ for the $N_z = 3$ verification data (shaded 68% CI regions). Other scales look qualitatively similar. Notably, the skewness systematically shifts our credible regions towards the long tails in direction of higher f_{δ} values because we report 68% intervals about the median posterior value. This shift for the cyan Z_3 regions can also be seen in random realisations of KiDS-1000 mock data, obtained by ray-tracing N -body simulations, in Fig. A.5.

The excellent fit of the model to the verification input data vector, \mathbf{d} , is best viewed in the posterior predictive plot, Fig. A.4. This plot compares the posterior model (blue regions for the two CIs 68% and 95% about the median) to the $\xi_{\pm}^{(ij)}(\theta)$ data points with 1σ error bars (black) as function of θ . The lower triangle of panels ‘ z - ij ’ shows $\theta \xi_{-}^{(ij)}$ for the tomographic bin pair (ij) , and likewise for the upper triangle and $\theta \xi_{+}^{(ij)}$. The data points scatter symmetrically about the median model at the centre of the CIs. Sometimes the residuals exceed 1σ or more, expected statistically for hundreds of (correlated) points. On the whole, we cannot see clear model shortcomings to match the verification data at any angular scale or redshift. This is underscored by the

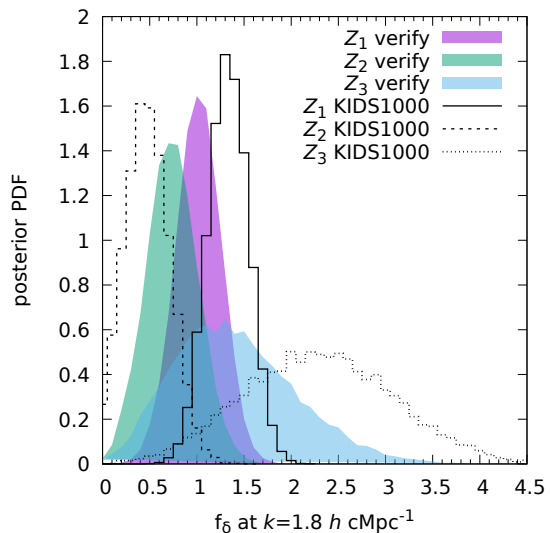


Fig. A.3. Posterior PDF of $f_{\delta, mn}$ at $k = 1.8 h \text{ Mpc}^{-1}$ in three separate redshift bins $Z_1 = [0, 0.3]$, $Z_2 = [0.3, 0.5]$, and $Z_3 = [0.6, 2]$. The filled regions are PDFs for a noisy verification run with $f_{\delta}(k, z) \equiv 1$, as in Fig. A.2, and the lines use the KiDS-1000 tomographic data (without marginalisation of projection parameters).

red solid lines for the true (fiducial) $\xi_{\pm}^{(ij)}(\theta)$: the red lines are well within the 68% CI, in dark blue, of the posterior model constraints. Figure A.6 is the same plot but for the actual KiDS-1000 data (Sect. 5.4 provides more details).

In summary, the foregoing tests demonstrate the excellent convergence of the Hamiltonian Monte-Carlo sampler used in the KiDS-1000 analysis and its ability to infer the 3D matter power spectrum with up to $N_z \times N_k = 60$ variables. More tests with $f_{\delta, mn} \neq 1$ verification data or mock data based on a CDM N -body simulation are presented in Sect. 3.2 and Sect. 5.5.

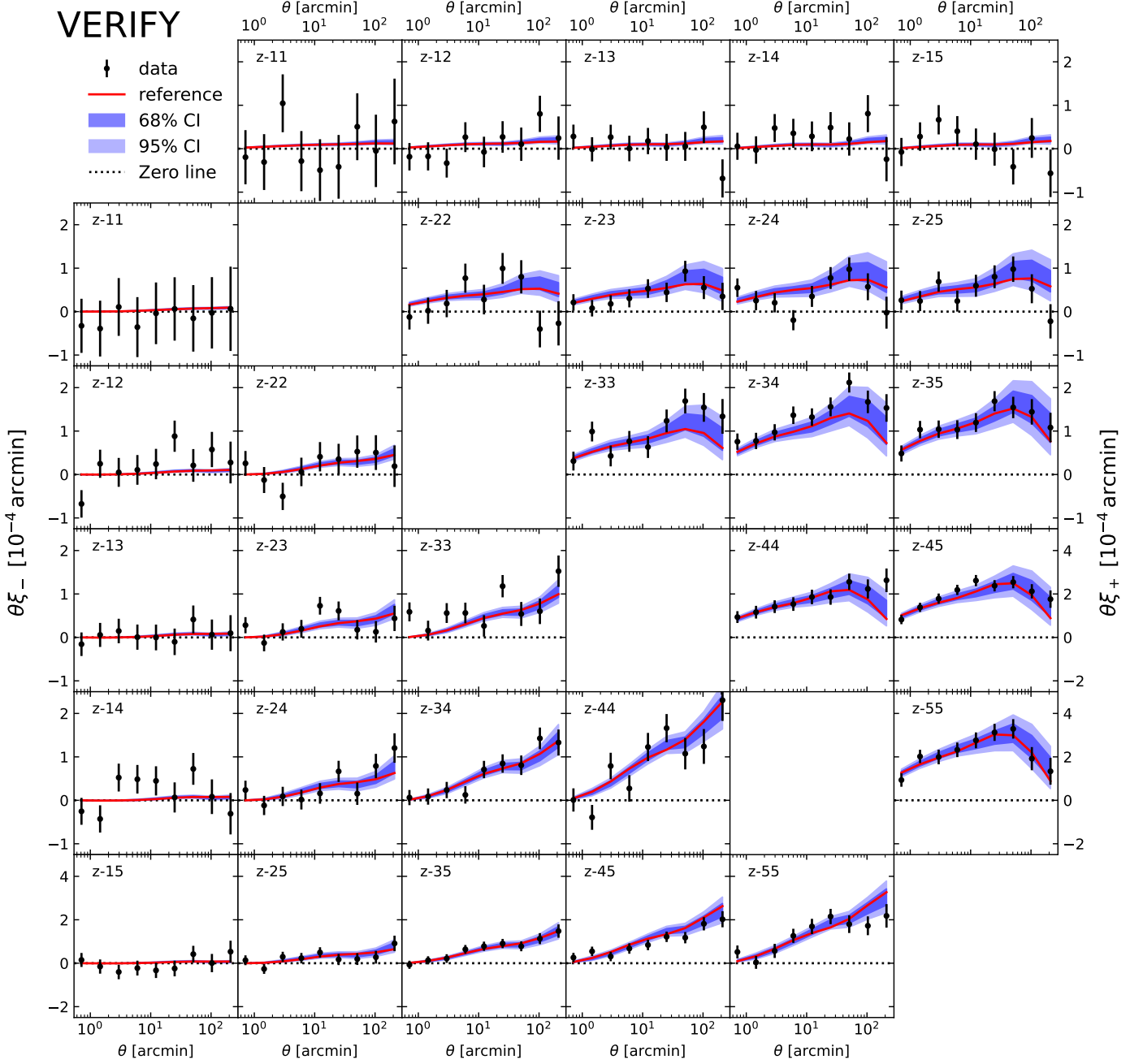


Fig. A.4. Same as in Fig. A.6 but here for a verification data vector (black points with errors bars), this means $f_{\delta,nn} \equiv 1$ by construction, with added random noise based on the error covariance matrix for KiDS-1000.

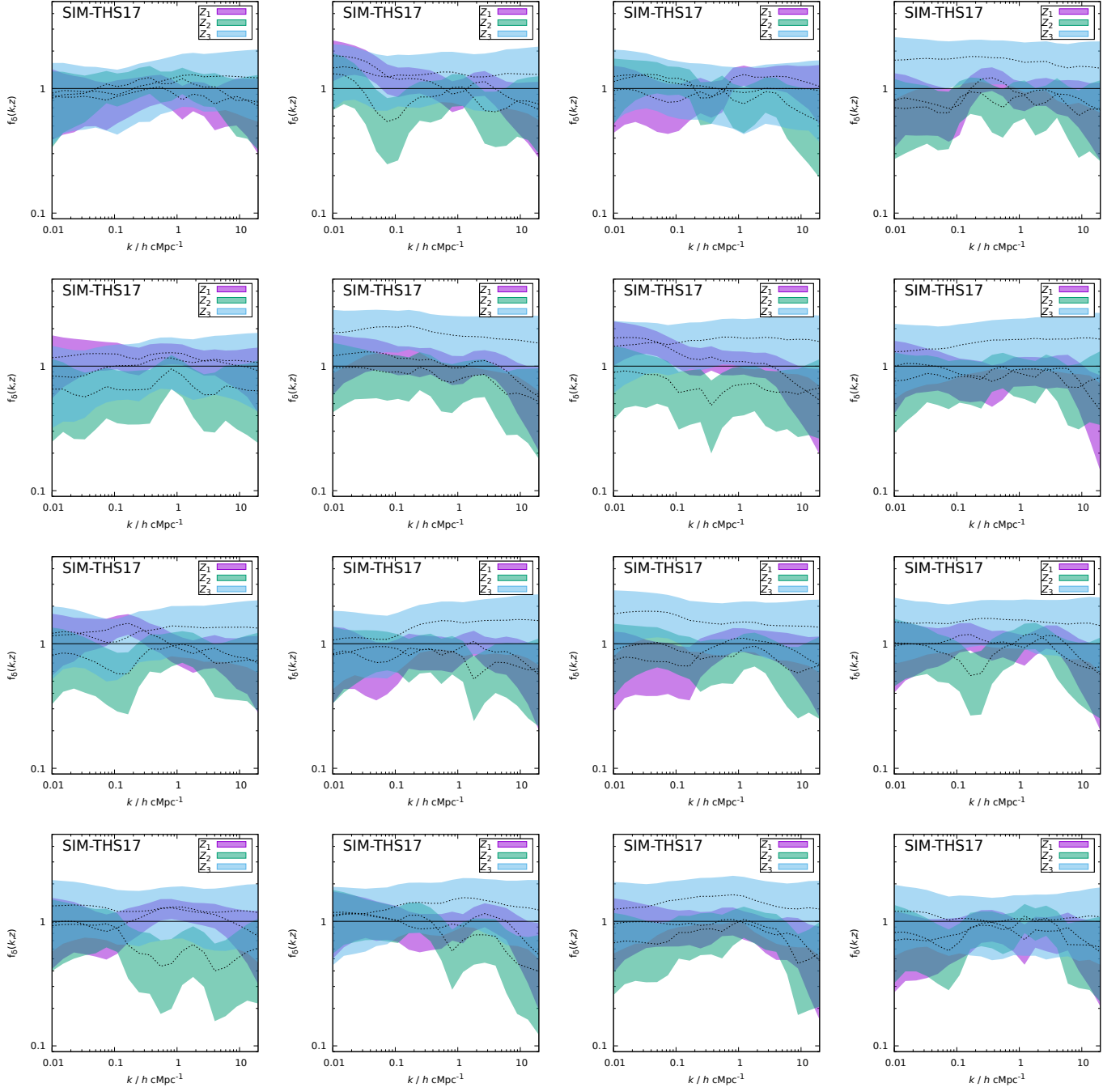


Fig. A.5. Illustration of possible variations in $f_{\delta}(k, z)$ reconstructions (68% CIs about the median) using noisy data vectors from the ray-traced KiDS-1000 mock-data which has $f_{\delta} \approx 1$ (Sect. 5.5). There is a tendency for $f_{\delta} > 1$ in $Z_3 = [0.6, 2]$ (cyan), and a tendency for $f_{\delta} < 1$ in $Z_2 = [0.3, 0.6]$ (green) due to skewed PDFs and correlated errors. The magenta region shows the constraints for $Z_1 = [0, 0.3]$ which are the tightest compared to Z_2 and Z_3 . An average over many reconstructions is shown in the bottom panel of Fig. 6.

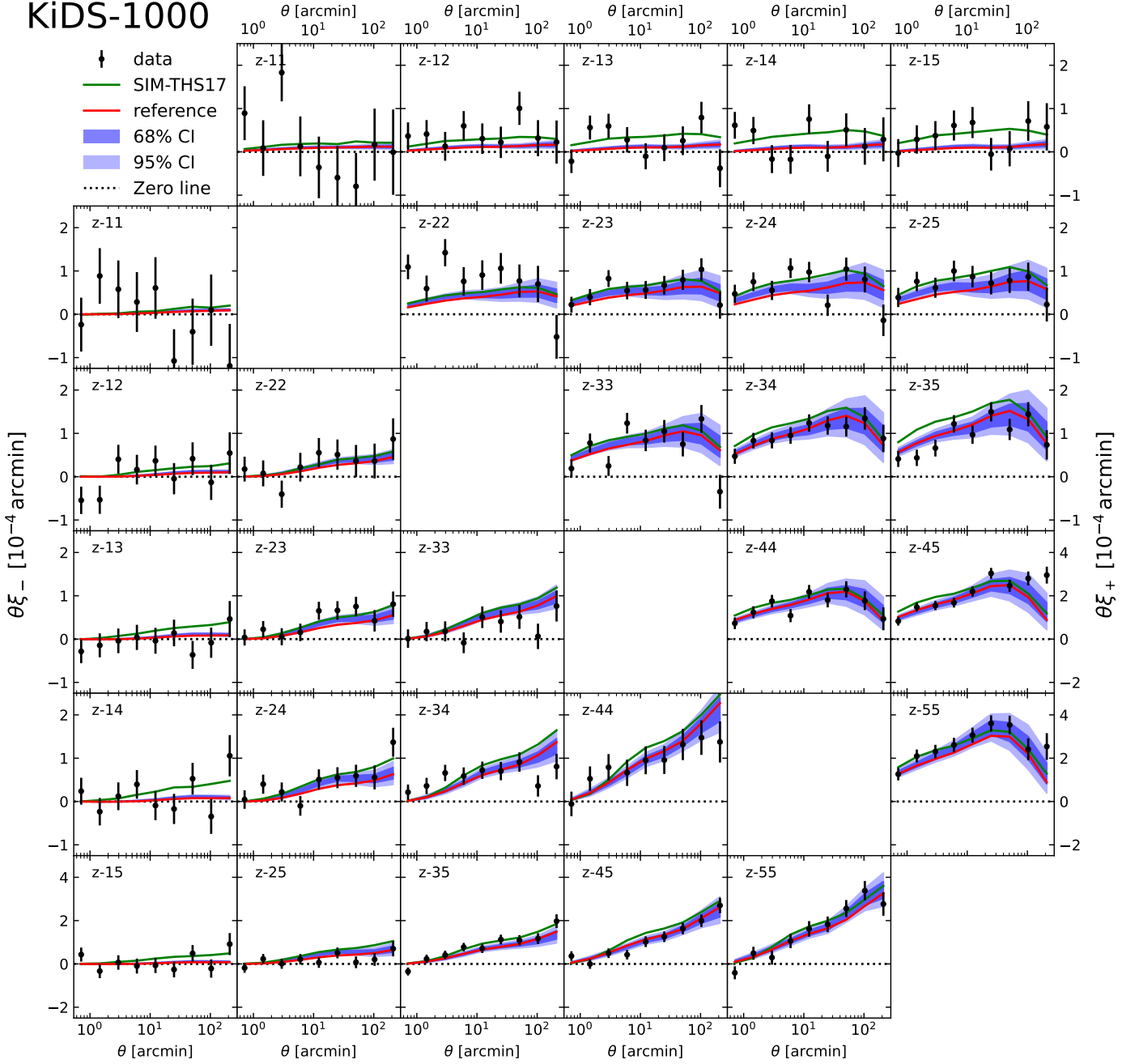


Fig. A.6. Posterior predictive of the Bayesian analysis using KiDS-1000 tomographic shear correlations and a relative power, $f_{\delta}(k, z)$, averaged inside the three redshift bins $Z_1 = [0, 0.3]$, $Z_2 = [0.3, 0.6]$, and $Z_3 = [0.6, 2]$. For each tomographic bin combination (ij), the panels with labels ‘ $z-ij$ ’ show the posterior model constraints as light blue (95% CI) regions and dark blue (68% CI) regions about the median for either $\theta \xi_{-}^{(ij)}(\theta)$ (lower left triangle) or $\theta \xi_{+}^{(ij)}(\theta)$ (upper right triangle), both in units of 10^{-4} arcmin and as function of lag θ . Black points with error bars (1σ) are the KiDS-1000 data points. The red lines correspond to the Λ CDM reference power spectrum with $S_8 \approx 0.72$, the solid green lines ‘SIM-THS17’ correspond to the prediction by Takahashi et al. (2017), see Sect. 5.5, for $S_8 \approx 0.79$. Errors of $\xi_{\pm}^{(ij)}(\theta)$ are correlated between θ -bins and tomographic bins, marginal errors due to lensing kernel and IA uncertainties are not included here (adding another $\sim 10\%$ to CIs). Conflicts with the data are visible for $\theta \xi_{+}^{(ij)}$ in $z-22$ and to a lesser degree for $z-12$ to $z-15$. Figure A.4 shows a random realisation of the reference model.

Table A.1. Overview of the KiDS-1000 ‘gold sample’

Bin	Redshift range	$n_{\text{eff}}/\text{arcmin}^{-2}$	σ_{ϵ}	δ_z^i
1	$0.1 < z_{\text{B}} \leq 0.3$	0.62	0.270	$+0.000 \pm 0.0106$
2	$0.3 < z_{\text{B}} \leq 0.5$	1.18	0.258	$+0.002 \pm 0.0113$
3	$0.5 < z_{\text{B}} \leq 0.7$	1.85	0.273	$+0.013 \pm 0.0118$
4	$0.7 < z_{\text{B}} \leq 0.9$	1.26	0.254	$+0.011 \pm 0.0087$
5	$0.9 < z_{\text{B}} \leq 1.2$	1.31	0.270	-0.006 ± 0.0097

Notes. The data in this table are compiled from Hildebrandt et al. (2021) and Giblin et al. (2021). The effective number density, n_{eff} , accounts for the *lensfit* weights, see Joachimi et al. (2021) for details. The fourth column displays the measured ellipticity dispersion per component. Our analysis takes into account the correlation of the redshift bias uncertainties.